



**HAL**  
open science

## **A viscoelastic model for human myocardium**

David Nordsletten, Adela Capilnasiu, Will Zhang, Anna Wittgenstein,  
Myrianthi Hadjicharalambous, Gerhard Sommer, Ralph Sinkus, Gerhard A  
Holzapfel

► **To cite this version:**

David Nordsletten, Adela Capilnasiu, Will Zhang, Anna Wittgenstein, Myrianthi Hadjicharalambous, et al.. A viscoelastic model for human myocardium. *Acta Biomaterialia*, In press, 10.1016/j.actbio.2021.08.036 . hal-03408971

**HAL Id: hal-03408971**

**<https://hal.science/hal-03408971>**

Submitted on 29 Oct 2021

**HAL** is a multi-disciplinary open access archive for the deposit and dissemination of scientific research documents, whether they are published or not. The documents may come from teaching and research institutions in France or abroad, or from public or private research centers.

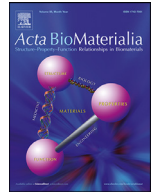
L'archive ouverte pluridisciplinaire **HAL**, est destinée au dépôt et à la diffusion de documents scientifiques de niveau recherche, publiés ou non, émanant des établissements d'enseignement et de recherche français ou étrangers, des laboratoires publics ou privés.



ELSEVIER

Contents lists available at ScienceDirect

Acta Biomaterialia

journal homepage: [www.elsevier.com/locate/actbio](http://www.elsevier.com/locate/actbio)

Full length article

## A viscoelastic model for human myocardium

David Nordsletten<sup>a,b,\*</sup>, Adela Capilnasiu<sup>a</sup>, Will Zhang<sup>c</sup>, Anna Wittgenstein<sup>a</sup>,  
Myrianthi Hadjicharalambous<sup>d</sup>, Gerhard Sommer<sup>e</sup>, Ralph Sinkus<sup>a,f</sup>, Gerhard A. Holzapfel<sup>e,g</sup>

<sup>a</sup> Division of Biomedical Engineering and Imaging Sciences, Department of Biomedical Engineering, King's College London, UK

<sup>b</sup> Departments of Biomedical Engineering and Cardiac Surgery, University of Michigan, North Campus Research Center, Building 20, 2800 Plymouth Rd, Ann Arbor 48109, MI, USA

<sup>c</sup> Department of Biomedical Engineering, University of Michigan, Ann Arbor, USA

<sup>d</sup> Department of Mechanical & Manufacturing Engineering, University of Cyprus, Nicosia, Cyprus

<sup>e</sup> Institute of Biomechanics, Graz University of Technology, Austria

<sup>f</sup> Inserm U1148, LVTS, University Paris Diderot, University Paris 13, Paris, France

<sup>g</sup> Department of Structural Engineering, Norwegian University of Science and Technology, Trondheim, Norway

### ARTICLE INFO

#### Article history:

Received 7 May 2021

Revised 22 August 2021

Accepted 24 August 2021

Available online xxx

#### Keywords:

Human ventricular myocardium

Viscoelasticity

Passive mechanical behavior

Cardiac mechanics

Tissue mechanics

Large deformation

### ABSTRACT

Understanding the biomechanics of the heart in health and disease plays an important role in the diagnosis and treatment of heart failure. The use of computational biomechanical models for therapy assessment is paving the way for personalized treatment, and relies on accurate constitutive equations mapping strain to stress. Current state-of-the-art constitutive equations account for the nonlinear anisotropic stress-strain response of cardiac muscle using hyperelasticity theory. While providing a solid foundation for understanding the biomechanics of heart tissue, most current laws neglect viscoelastic phenomena observed experimentally. Utilizing experimental data from human myocardium and knowledge of the hierarchical structure of heart muscle, we present a fractional nonlinear anisotropic viscoelastic constitutive model. The model is shown to replicate biaxial stretch, triaxial cyclic shear and triaxial stress relaxation experiments (mean error  $\sim 7.68\%$ ), showing improvements compared to its hyperelastic (mean error  $\sim 24\%$ ) counterparts. Model sensitivity, fidelity and parameter uniqueness are demonstrated. The model is also compared to rate-dependent biaxial stretch as well as different modes of biaxial stretch, illustrating extensibility of the model to a range of loading phenomena.

### Statement of Significance

The viscoelastic response of human heart tissues has yet to be integrated into common constitutive models describing cardiac mechanics. In this work, a fractional viscoelastic modeling approach is introduced based on the hierarchical structure of heart tissue. From these foundations, the current state-of-the-art biomechanical models of the heart muscle are transformed using fractional viscoelasticity, replicating passive muscle function across multiple experimental tests. Comparisons are drawn with current models to highlight the improvements of this approach and predictive responses show strong qualitative agreement with experimental data. The proposed model presents the first constitutive model aimed at capturing viscoelastic nonlinear response across multiple testing regimes, providing a platform for better understanding the biomechanics of myocardial tissue in health and disease.

© 2021 Acta Materialia Inc. Published by Elsevier Ltd. All rights reserved.

\* Corresponding author at: Departments of Biomedical Engineering and Cardiac Surgery, University of Michigan, North Campus Research Center, Building 20, 2800 Plymouth Rd, Ann Arbor 48109, MI, USA.

E-mail address: [nordslet@umich.edu](mailto:nordslet@umich.edu) (D. Nordsletten).

## 1. Introduction

The biomechanical function of the human heart is a critical component of cardiac physiology. Beyond the role of its active properties leading to contraction of the myocardium, the passive characteristics of heart muscle play a key role in cardiac pathophysiology, particularly in conditions such as diastolic heart fail-

ure [1], heart failure with preserved ejection fraction (HFpEF) [2], and myocardial infarction [3]. Patients with these conditions often have poor outcomes due, in part, to patient variability and current challenges in predicting therapy efficacy. Cardiac biomechanical modeling provides a tool for addressing these needs, providing the capacity for patient-specific assessment and model predicted outcomes. These models are playing an increasingly important role in translational cardiac modeling [4] and rely on appropriate constitutive models to predict the passive biomechanical response of the myocardium throughout the cardiac cycle.

Constitutive model characterization of passive myocardial tissue has been a focus of research for over 1.5 centuries [5,6]. Experimental studies in animals have shown that myocardial tissue exhibits nonlinear stress-strain response [7], anisotropy in biaxial stretch [8,9,10], and orthotropy under shear [11,12]. Recently, these effects were extended and shown in bovine [13,14] and human myocardial tissue [15,16]. These experimental insights have driven the development of numerous mechanical constitutive models, with varying degrees of fidelity [4]. In most cases, myocardial models have leveraged hyperelasticity theory [17,18,19], defining the stored energy (strain-energy) in response to the loading of muscle tissue. Efforts at developing constitutive relations largely paralleled available data, with early descriptions focusing on transversely isotropic strain-energy equations [20,21,9,22], followed by orthotropic descriptions [23,24,25,26]. In the hyperelastic formulation, the transfer from external energy to internal energy (or *vice versa*) is lossless, providing perfect energetic retention and return.

While current models treat the heart muscle as hyperelastic, this belies the considerable evidence of myocardial viscoelasticity. Viscoelastic response has long been observed in muscle tissue, with early evidence stemming from the work of Blix [5,27,28] who showed hysteresis in *ex vivo* frog gastrocnemius. This loss was further characterized by Hill and Hartree [29], who demonstrated the loss of energy in the stretch and relaxation of viable/non-viable muscle tissue samples. These *viscous elastic* effects were initially explained using a *spring and dashpot* model by Levin and Wyman [30]. Hysteresis and nonlinear stress-strain relations were later demonstrated in the canine papillary by Walker [31] and at the organ-scale in the Langendorff feline heart experiments of Leach and Alexander [32]. Viscoelastic relaxation phenomena were observed in the *ex vivo* beating tortoise heart by O'Brien and Remington [33]. Similar experiments were studied in conscious dogs, demonstrating hysteresis and creep *in vivo* [34]. A comprehensive mechanical assessment was later performed in the rabbit papillary muscle by Pinto and Fung [7], showing relaxation, creep, hysteresis along with a modest frequency dependence. Since, viscoelastic behaviors have been reported in many experimental works [8,10–12,15,16].

The role of viscoelasticity in myocardial mechanics, while clear experimentally, has yet to be widely adopted by the constitutive equations for heart tissue. This is, in part, due to the already complex nature of state-of-the-art cardiac mechanics models – involving multiple nonlinear anisotropic terms with multiple unknown parameters. In addition, the lack of straightforward nonlinear viscoelastic models to build from has limited their extension. A range of rheological analyses have been performed [35], and used as the basis for linear viscoelastic models (see, e.g., [36–38]). These efforts were soon extended into nonlinear elasticity theory by Coleman and Noll [39], Truesdell and Noll [40,19], Pipkin and Rogers [41], and extended to quasi-linear viscoelasticity for biological tissues by Fung [37] (see the review by Wineman [42]). Efforts moving nonlinear viscoelastic models into simulations were done by Simo [43] and Holzapfel [44–46]. Extension of these approaches to the nonlinear viscoelastic behavior in the heart were presented by Huyghe et al. [47] and Cansiz et al. [48]. Recently, a study by Gültekin et al. [49] used an analogue to the Maxwell-Wierchert model

to characterize viscoelastic effects in the different microstructural orientations, providing the first three-dimensional anisotropic nonlinear viscoelastic constitutive equation for human myocardial tissues. Interestingly, however, the model required significantly different parameter sets and relaxation times depending on the experiment performed by Sommer et al. [15,16].

Here we present a three-dimensional viscoelastic constitutive model framework for the human myocardium. A structural argument is presented based on the hierarchical nature of the myocardial tissue, suggesting the presence of a spectrum of relaxation times. Following the previous works of Simo and others [43,44,46] as well as extensions to fractional approximations [50,51], a fractional anisotropic nonlinear viscoelastic model is proposed that encapsulates phenomena observed in the heart. The model developed for myocardium is fit to recent human myocardial data [15,16], showing mean errors of  $\sim 7.68\%$  compared to  $\sim 24\%$  for hyperelastic variants. Moreover, the model is used to predict variations of biaxial stretch and stretch rate, showing compelling predictions of the passive muscle response. The developed model uses 11 parameters (compared to 17 and 18 used in [48,49]), which are shown to be unique. This model represents the first nonlinear anisotropic viscoelastic model of human myocardium demonstrated to fit the biomechanical response of myocardial tissue and show reasonable predictions of tissue response.

Outlining the work, we begin by reviewing the potential sources of myocardial viscoelasticity, building a structural argument that provides the foundation of the model (Section 2.1). Basic notation and hyperelastic formulations for cardiac mechanical models are reviewed (Sections 2.2 and 2.3). From these foundations the anisotropic nonlinear viscoelastic power law model for the human myocardium is introduced (Sections 2.4–2.6). Sections 2.7 and 2.8 review the human rheological data used in this study as well as the parameterization procedure followed. Results of the model are then presented in Section 3, with discussion presented in Section 4.

## 2. Materials and methods

### 2.1. Origins of viscoelasticity in passive myocardium

The complex structure of myocardial tissue has led to discussion over the origins of viscoelasticity. Many constituent components of the myocardium have been implicated as the source of viscoelasticity, including tissue perfusion, extracellular fluid, myocytes, the extracellular matrix (ECM) and others. Simulated poromechanical studies [52] have demonstrated that tissue perfusion can yield stress relaxation. Increased extracellular fluid content is known to significantly influence the biomechanics of tissues [53–55]. Experimental studies on sarcomeres have demonstrated that the primary contractile proteins of the heart exhibit passive viscoelastic behavior [56]. Studies have also shown that the main constituents of the ECM exhibit viscoelasticity [57], suggesting molecular friction as a source of viscoelastic response. While these factors are often considered and advocated for individually, it is highly likely that all factors can contribute to the viscoelastic response of the myocardium with varying degrees of importance depending on the spatiotemporal scales and loading conditions considered. In the following section, we review the evidence for these different factors contributing to the viscoelastic response of myocardial tissue.

#### 2.1.1. Influence of tissue perfusion and extracellular fluid

Due to the surrounding interstitial fluid space and the perfusion of myocardial tissues by the coronary vasculature, it is clear that the heart is a complex poromechanical organ. Debate then arises whether the viscoelastic behavior observed predominantly

stems from fluid movement through the porous tissue (*i.e.* the tissue is nearly poroelastic) or if the solid compartment itself is viscoelastic (*i.e.* the tissue is poroviscoelastic). Questions also arise regarding the influence of these effects *in vivo* versus the typical testing environment *ex vivo*. In multiple tissue studies [11–13,16], non-perfused tissues exhibited significant viscoelastic response. While this could be explained by the movement of interstitial fluid, the shear rates required to dissipate the energy observed experimentally would require much larger frequencies and would not explain the seemingly nonlinear loss response observed. This was shown through modeling by Yang and Taber [52], who demonstrated that the viscoelastic response due to poroelasticity was not sufficient to explain hysteresis observed in data. However, the presence of extracellular fluid and vasculature has a clear influence on the biomechanics of tissue, with results showing that a change in the aqueous solution directly impacts apparent stiffness [58]. Hydration of myocytes and the ECM proteins both have significant impacts on their properties and viscoelasticity, making these factors critical to the passive behavior of tissue. Further, in simulation studies [59], it was shown that pore pressure yields a generalized stiffening by loading the ECM which could, in turn, influence viscoelastic response of structural proteins. As a consequence, the viscoelastic response of tissue is inextricably linked to the constituents of the extracellular environment whether (or not) the porous flow of fluid plays a leading role in the viscoelastic mechanical response observed.

### 2.1.2. Influence of cardiomyocytes

The passive mechanics of cardiomyocytes have also been identified as contributors to viscoelastic response. The viscoelastic impact of myocytes is often thought to be significant due to the encapsulated fluid of the cytosol. However, skinned myocytes exhibit strong passive viscoelastic response, thought to arise from molecular friction in the macromolecules such as titin [60]. In addition, intracellular structural proteins, such as actin [61], have also exhibited viscoelasticity due to molecular friction. While myocytes exhibit passive viscoelastic response, it is unclear the degree to which passive cellular forces contribute to the total tissue response. Witzenburg et al. [62] demonstrated that decellularization of rat myocardium increased the apparent stiffness of the myocardium 6.7 fold in biaxial tests; an increase that corresponded to the 5.6 fold reduction in cross-sectional area. While this may suggest that cells provide a minor contribution to passive biomechanics, it is clear that the turgid cylinder-like structure of the cardiomyocyte plays a significant role in resistance to shear and compression.

### 2.1.3. Influence of extracellular matrix structure

The extracellular matrix is acknowledged as a critical, and dominant, component of passive mechanical properties in the heart [63–65]. The ECM is highly hierarchical [66] (see Fig. 1), exhibiting important structural organization at multiple scales. A fundamental building block of myocardial ECM are collagen I and III [67] (approximately 300 nm in length). The extremely rigid collagen molecule triple helices are bound to form collagen fibrils, with diameters of 10–500 nm and lengths on the order of 10–30  $\mu\text{m}$  (see Fig. 2A). This structural arrangement provides opportunity for significant molecular interaction, yielding potential molecular friction mechanisms as molecules translate relative to one another. Indeed, Shen et al. [57] performed stress relaxation experiments on individual collagen (type I) fibrils, demonstrating viscoelastic response. Characterization of this relaxation response required a 2-component Maxwell-Weichert model, suggesting multiple relaxation times are present at the scale of individual fibrils. It has also been shown that collagen fibrils exhibit nonlinear re-

sponse, stemming from an uncoiling of end groups leading to progressive recruitment of molecules [68,69].

Collagen fiber formation bundles together many individual fibrils. Fiber bundles vary significantly in diameter (with type I forming larger bundles than type III) and can span over extended distances. To avoid rigid locking between fibrils, a layer of proteoglycans and glycosaminoglycans cover the outer fibril surface [70] (see Fig. 2B). These large proteins are strongly hydrophilic, binding with water and enabling molecular lubrication between fibrils. Collagen fibers are then linked together to other collagen molecules, often running in close proximity through myocardial tissue (see Fig. 2C).

At the tissue scale, fibers weave together forming the ECM (see Fig. 1). Fibers form complex layers of endomysial collagen – surrounding and spanning between individual myocytes – and perimysial collagen – surrounding and spanning between muscle sheets (see Fig. 2D). Endomysial and perimysial collagen exhibit a complex structure that undergoes predictable molecular realignment and uncoiling under load [71–73]. Stretch of individual cells requires deformation of the endomysial layer, resulting in molecular friction as fibers translate relative to one another. Scaling up to the level of myocardial sheets, a similar process of deformation and relative translation occurs within the perimysial layer.

Examining the hierarchical structure of the ECM, it is clear that molecular friction and potential drivers of viscoelastic response are pervasive and present at multiple spatial scales. From fibril to fiber to collagen layers, a relative translation of molecules to macromolecular complexes can be observed. The multiscale mechanisms of molecular friction suggest that myocardial tissue is likely characterized by a spectrum of relaxation events occurring at a broad range of time-scales. This is in contrast to some collagen hydrogels which can exhibit less orderly structure [74,75] and can be well characterized by a simple series of relaxation times [76–79].

## 2.2. Kinematics and notation

Here, we briefly introduce the classic kinematic notation used in nonlinear mechanics (see, *e.g.*, [17,18,80]). Deformation in the heart can be defined by the motion of material points as they move from their reference,  $\Omega_0 \subset \mathbb{R}^3$ , to their physical configurations,  $\Omega_t \subset \mathbb{R}^3$  (at some time  $t \in [0, T]$ ). Marking material points of the reference domain by their coordinate position,  $\mathbf{X} \in \Omega_0$  (with the gradient operator,  $\nabla_{\mathbf{X}}$ ), the relative motion is defined by the displacement field  $\mathbf{u} : \Omega_0 \times [0, T] \rightarrow \mathbb{R}^3$  whereby  $\mathbf{x}(\mathbf{X}, t) = \mathbf{u}(\mathbf{X}, t) + \mathbf{X}$ . Local deformation of material axes and volumes is characterized by the deformation gradient,  $\mathbf{F} = \nabla_{\mathbf{X}}\mathbf{x} + \mathbf{I}$ , and its determinant,  $J = \det \mathbf{F} > 0$ , respectively [18]. Often, the heart is approximated as an incompressible tissue (*e.g.*,  $J = 1$ ), though debate about this exists in the literature [81]. Measures of stretch are given by the right and left Cauchy Green tensors, defined as  $\mathbf{C} = \mathbf{F}^T \mathbf{F}$  and  $\mathbf{B} = \mathbf{F} \mathbf{F}^T$ , respectively.

Often it is convenient to define constitutive relations using invariants of stretch / strain tensors (here generically denoted by  $\mathbf{A}$ ) given by Bonet and Wood [17]

$$I_{\mathbf{A}} = \mathbf{A} : \mathbf{I}, \quad II_{\mathbf{A}} = \mathbf{A} : \mathbf{A}, \quad III_{\mathbf{A}} = \det \mathbf{A}. \quad (1)$$

It can also be convenient to consider isochoric invariants, replacing  $\mathbf{A}$  with  $\bar{\mathbf{A}} = \mathbf{A} / III_{\mathbf{A}}^{1/3}$  in Eq. (1) (*e.g.*,  $\bar{I}_{\mathbf{A}} = \bar{\mathbf{A}} : \mathbf{I}$ ), as these can facilitate the isochoric / deviatoric split in hyperelastic formulations.

Considering anisotropic materials, such as myocardium, a common approach is to define mutually orthogonal local microstructural directions,  $\{\mathbf{e}_f, \mathbf{e}_s, \mathbf{e}_n\}$ , at each material point. Here  $\mathbf{e}_a$  denotes the unit orientation vector along myofibers (f), sheets (s) and sheet normals (n) [82]. The physical (deformed) orientation of these microstructural directions are given by  $\mathbf{e}_a = \mathbf{F} \mathbf{e}_a$ ,  $a \in \{f, s, n\}$ . Hence, the squared stretch along microstructural directions can be

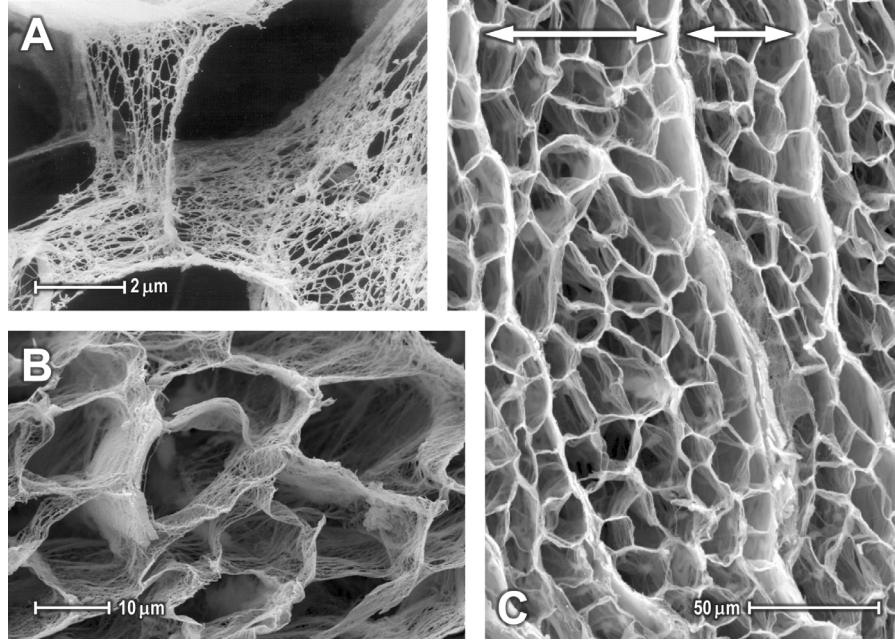


**Fig. 1.** Scanning electron microscopy of ECM structure in the (A) rabbit and (B,C) canine myocardium. (A) Illustrates the detailed microstructure and collagen fibers composing the endomysial collagen layer that normally surrounds and interlinks cardiomyocytes. (B) Shows magnification of the ECM structure, showing pockets normally encasing multiple myocytes as well as the coronary microvasculature. (C) Magnification of the ECM, showing myocardial sheets separated by perimysial collagen layers (marked with arrows). Reproduced with permission from Benedicto et al. [101,102].

expressed by the pseudo invariants,

$$I_a = \mathbf{C} : \mathbf{e}_a \otimes \mathbf{e}_a = \mathbf{e}_a \cdot (\mathbf{C}\mathbf{e}_a) = \mathbf{e}_a \cdot \mathbf{e}_a, \quad a \in \{f, s, n\}. \quad (2)$$

Generalizing Eq. (2),

$$I_{ab} = \mathbf{C} : \text{sym}(\mathbf{e}_a \otimes \mathbf{e}_b) = \mathbf{e}_a \cdot \mathbf{e}_b, \quad a, b \in \{f, s, n\}, \quad (3)$$

where  $\text{sym}(\mathbf{A}) = \frac{1}{2}(\mathbf{A} + \mathbf{A}^T)$  is the symmetric transformation. These invariants play an important role in defining the constitutive behavior in myocardial tissue [24].

### 2.3. Hyperelastic formulations of the myocardium

Though a number of constitutive equations have been developed to describe myocardial tissue [24–26], in this study we focus on two of the most common orthotropic models, the Holzapfel and Ogden [24] (*HO*) and the Costa [23] models. The *HO* model is a hyperelastic incompressible strain-energy function, widely employed in modeling studies and is appealing for both theoretical reasons (e.g., convexity and objectivity) as well as parameter identifiability [83,26]. Recalling briefly, the incompressible *HO* strain-energy  $W_e : \mathbb{R}^{3 \times 3} \times \mathbb{R} \rightarrow \mathbb{R}_{\geq 0}$  can be written as

$$W_e(\mathbf{C}, p) = W_{iso}(\bar{\mathbf{C}}) + W_{ff}(I_{ff}) + W_{ss}(I_{ss}) + W_{fs}(I_{fs}) + p(J - 1), \quad (4)$$

where

$$W_{iso}(\bar{\mathbf{C}}) = \frac{a}{2b} [\exp\{b(\bar{\mathbf{C}} - 3)\} - 1], \quad (5)$$

$$W_{kl}(I_{kl}) = \frac{a_{kl}}{2b_{kl}} [\exp\{b_{kl}(I_{kl} - \delta_{kl})^2\} - 1], \quad (6)$$

and  $\delta_{kl}$  denotes the Kronecker delta (zero unless  $k = l$ , in which case it is 1). In this formulation, the strain-energy is written as a sum of components. The isotropic term,  $W_{iso}$ , provides the isotropic bulk distortional energy associated with tissue deformation. Anisotropic terms  $W_{kl}$  (where  $k, l \in \{f, s, n\}$ ) are introduced to account for the varying distortional energy associated with deformation along microstructural directions. We note that the

anisotropic invariants  $I_{ff}$  and  $I_{ss}$  are thought to not support compression, hence making the anisotropic strain-energy terms zero when  $I_{ff}, I_{ss} < 1$  [24]. We note, in the tests considered here, neither  $I_{ff}$  nor  $I_{ss}$  are in compression. In the *HO* model, the set of anisotropic terms depend on 8 fitting parameters (denoted by  $a$ 's and  $b$ 's). In the *HO* model, the second Piola Kirchhoff stress (PK2)  $\mathbf{S}$  can be written as

$$\mathbf{S} = \frac{2}{J^{2/3}} \frac{\partial W_{iso}}{\partial \bar{\mathbf{C}}} \left( \mathbf{I} - \frac{I_{\mathbf{C}}}{3} \mathbf{C}^{-1} \right) + \sum_{kl \in S} 2 \frac{\partial W_{kl}}{\partial I_{kl}} \text{sym}(\mathbf{e}_k \otimes \mathbf{e}_l) + \mathbf{S}_p, \quad (7)$$

with  $S = \{ff, ss, fs\}$  and  $\mathbf{S}_p = pJ\mathbf{C}^{-1}$ . Through push forward operations (i.e.,  $\boldsymbol{\sigma} = J^{-1}\mathbf{F}\mathbf{S}\mathbf{F}^T$ ), the second Piola Kirchhoff stress tensor can be extended into the Cauchy stress tensor. We note that the original *HO* formulation considered the strain-energy defined using standard invariants [24], with later forms defined using isochoric invariants and/or dispersion [49].

Another constitutive equation that is widely employed is the Costa model [23]. This model is well-posed in terms of convexity and objectivity [24] and relies on an orthotropic formulation of the exponential Fung-type law. While typically written in terms of rotated Green Lagrange strain tensors, the Costa model can similarly be expressed in terms of invariants of the right Cauchy Green strain tensor, e.g.

$$W = \frac{C}{4} [\mathcal{W}(\mathbf{C}) - 1] + p(J - 1), \quad \mathcal{W}(\mathbf{C}) = \prod_{kl \in S'} W'_{kl}(I_{kl}), \quad (8)$$

where

$$W'_{kl}(I_{kl}) = \exp\{b_{kl}(I_{kl} - \delta_{kl})^2\}, \quad (9)$$

and  $S' = \{ff, ss, nn, fs, fn, sn\}$ . This form is useful for comparison of these models, illustrating that the Costa model shares the same underlying exponential invariant formulation; however, strain-energy terms are grouped in one term  $\mathcal{W}(\mathbf{C})$ , through multiplication. In this case, the Costa model is comprised of 7 material parameters, an outer scaling constant,  $C$ , along with anisotropic

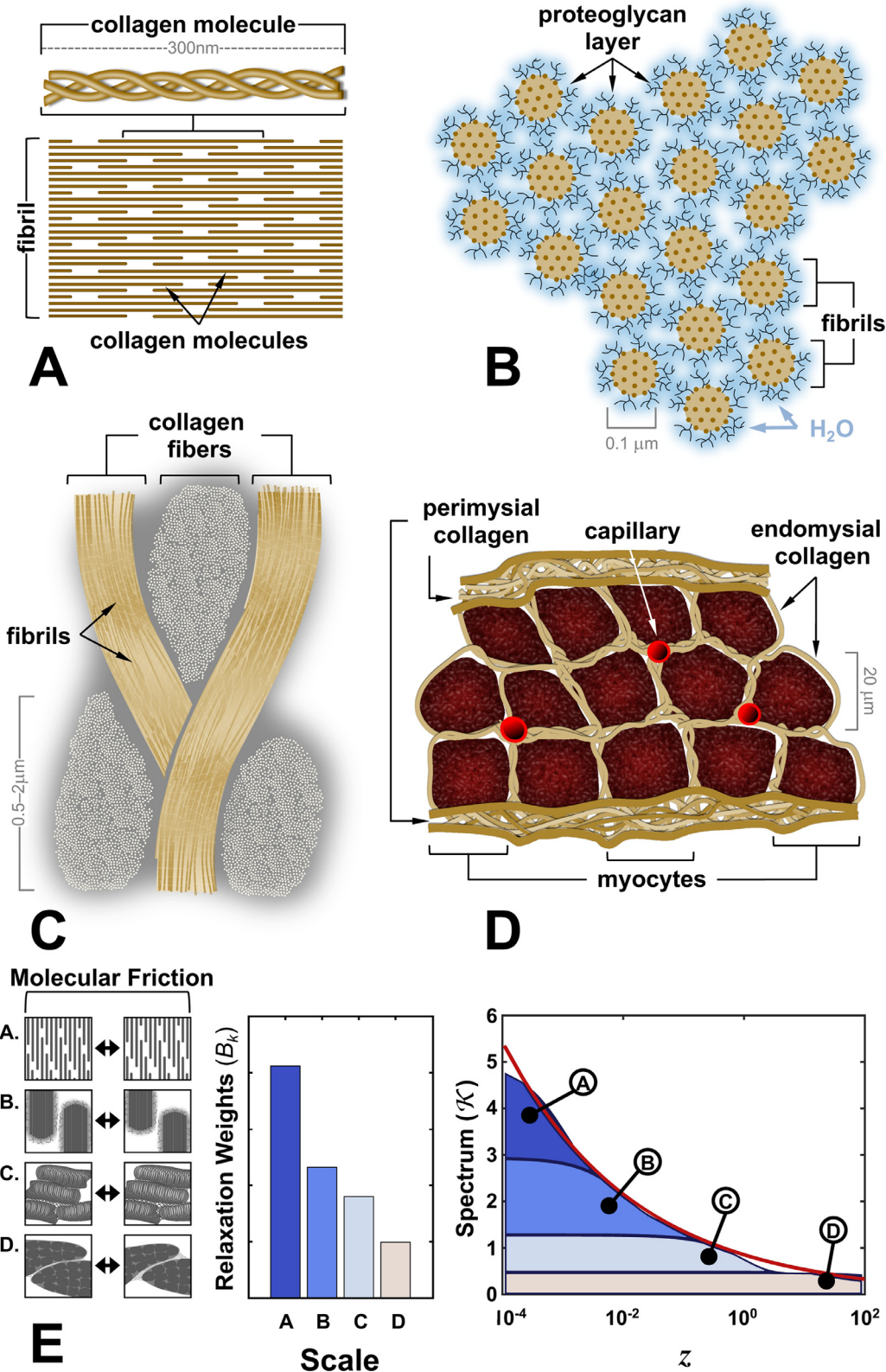


**Fig. 2.** Schematic representation of the hierarchical structure of the extracellular matrix, and its representation as a power spectrum. (A) Illustration of the collagen triple helix and structural arrangement of the collagen fibril. (B) Illustration of the lattice arrangement of fibrils within a collagen fiber, showing fibrils, proteoglycans and their hydration. (C) Illustration of bundled fibrils within collagen fibers and their cross section. (D) Illustration of the myocardial tissue showing myocytes and capillaries surrounded by endomysial collagen fibers and encased in sheets covered by perimysial collagen. (E) Illustration of multiscale friction processes yielding a fractional relaxation response moduli. (Left) Sketch of multiscale friction processes (A) within fibrils, (B) between fibrils, (C) at the endomysial collagen scale, and (D) at the perimysial collagen scale. (Middle) Effective density of relaxation phenomena within a representative volume. (Right) Combined multiscale relaxation response modulus with colors indicating different scales of response and its representation using a fractional model where  $\mathcal{K}(z) \propto z^{-\alpha}$  (red curve). (For interpretation of the references to color in this figure legend, the reader is referred to the web version of this article.)

scaling constants,  $b$ . The PK2 stress tensor can be written as

$$\mathbf{S} = C\mathcal{W}(\mathbf{C}) \sum_{kl \in S'} b_{kl} (I_{kl} - \delta_{kl}) \text{sym}(\mathbf{e}_k \otimes \mathbf{e}_l) + \mathbf{S}_p. \quad (10)$$

Both *HO* and *Costa* models utilize exponential forms commonly employed in collagenous biological tissues [68,69] reflecting the toe, heel and linear regime of collagen fibrils and the progressive recruitment of coiled fibers with stretch. Further, while in this paper we focus on incompressible forms, both models have been used considering the myocardium as compressible (or nearly incompressible), where  $\mathbf{S}_p$  is replaced with an appropriate compressibility term. The primary variation between models is the separable form employed in *HO* compared to the coupled exponential form of the *Costa* model. Both model forms have advantages and disadvantages in terms of model performance and parameter identifiability.

#### 2.4. Extension to cardiac viscoelasticity

Viscoelastic phenomena in muscles have been described using a range of linear spring, dashpot and spring pot system models [30,84]. One of the simplest models that captures stress relaxation (impulse stretch) and creep (impulse stress) is the Zener model, containing a Maxwell model in parallel with a spring (cf. [36,18]). Denoting the stress in the elastic branch of the model as  $\sigma_0^e(t) = E_0 \varepsilon(t)$ , the total stress in the Zener model can be written as

$$\sigma(t) = \sigma_0^e(t) + \int_0^t B \exp\{(s-t)/\tau\} \dot{\sigma}_0^e(s) ds \quad (11)$$

where  $\tau = (E/\eta)^{-1}$  is the relaxation time,  $B = E/E_0$  is the relaxation weight and  $E$  and  $\eta$  are the elastic and viscous moduli of the Maxwell branch [35]. In this model, the asymptotic elastic response is given by the first term, while the viscoelasticity is encapsulated in the second term. Eq. (11) provides a template for defining the stress response [85]. Extending this idea to nonlinear materials, a straightforward approach is to replace the elastic stress component  $\sigma_0^e$  with its nonlinear hyperelastic variants. Replacing  $\sigma_0^e$  with an appropriate nonlinear PK2 form  $\mathbf{S}_e$ , yields the quasi-linear viscoelastic (QLV) Fung model,

$$\mathbf{S}(t) = \mathbf{S}_e(t) + \int_0^t \mathcal{K}(s-t) \dot{\mathbf{S}}_e(s) ds + \mathbf{S}_p(t), \quad (12)$$

where, for the Zener model,  $\mathcal{K}(s-t) = B \exp\{(s-t)/\tau\}$ . Here the QLV Fung model extension is considered linear due to the linear dependence on  $\mathbf{S}_e$ . As noted in Section 2.1, myocardial tissue is strongly influenced by viscoelastic phenomena across a hierarchy of scales, with collagen fibrils themselves exhibiting multiple relaxation times [57]. A straightforward adaptation is to consider a nonlinear variant of the Maxwell-Wiechert model (or Generalized Maxwell model) [86,87]. Considering  $n$  viscoelastic elements in parallel, due to linearity, this could be modeled simply by altering the QLV form, with the relaxation

$$\mathcal{K}(s-t) = \sum_{k=0}^n B_k \exp\{(s-t)/\tau_k\}. \quad (13)$$

Here,  $B_k$  and  $\tau_k$  represent the relaxation weights and relaxation times of the various viscoelastic elements. Note that, here, we have assumed that the branches share the same nonlinear form  $\mathbf{S}_e$ , which need not be the case. In the limit as the number of branches gets increasingly large, the relaxation response modulus can be considered as a continuous distribution across relaxation times, rewriting the sum as an integral over the reciprocal  $\xi = 1/\tau$  with a continuous relaxation weight  $B = B(\xi)$  representing the proportional influence of a given relaxation time, e.g.

$$\mathcal{K}(s-t) = \int_0^\infty B(\xi) \exp\{(s-t)\xi\} d\xi. \quad (14)$$

In this form, the continuous relaxation response modulus is simply the Laplace transform of the continuous relaxation weight  $B(\xi)$ , e.g.  $\mathcal{L}\{B; t-s\}$ . While this form provides generality for encapsulating the viscoelastic response of a material in the QLV framework, it also requires unique determination of all the relaxation weights and times or relaxation weight spectrum itself, which is challenging to obtain experimentally particularly for nonlinear anisotropic materials like the myocardium. However, if these weights and time constants were distributed in a well-characterized way, it's possible that the spectrum could follow a simplified approximate form.

#### 2.5. Extension to fractional viscoelasticity

Fractional viscoelasticity – a class of viscoelastic models – has been shown to capture some of the key viscoelastic behaviors of soft tissues [50,35,88,89] across a range of tissues. Fractional viscoelasticity can be closely related to the generalized Maxwell model, where the relaxation behavior is comprised of multiple exponential decay terms such that  $\mathcal{K}(s-t) \propto (t-s)^{-\alpha}$  (see Fig. 2). Formally, the fractional model can be thought of as an infinite series of exponential decay terms where the relaxation weight  $B(\xi) = B_0 \xi^{\alpha-1} \sin(\pi\alpha)/\pi$ , for some constant  $B_0 > 0$  and  $\alpha \in (0, 1)$ . Substitution of this form into Eq. (14) simplifies  $\mathcal{K}(s-t) = B_0 (t-s)^{-\alpha} / \Gamma(1-\alpha)$ , resulting in the fractional viscoelastic form

$$\mathbf{S}(t) = \mathbf{S}_e(t) + B_0 D_t^\alpha \mathbf{S}_e + \mathbf{S}_p(t), \quad (15)$$

where  $D_t^\alpha$  denotes the  $\alpha$ -order Caputo derivative [90]

$$D_t^\alpha g = \frac{1}{\Gamma(1-\alpha)} \int_0^t (t-s)^{-\alpha} \dot{g}(s) ds, \quad \alpha \in [0, 1]. \quad (16)$$

Here,  $B_0$  modulates the relative strength of the viscoelastic response, while  $\alpha$  modulates the distribution of relaxation times. Conceptually, the fractional model represents a material with a continuous viscoelastic relaxation spectrum, where  $\mathcal{K}$  is weighted for long timescales ( $\alpha \rightarrow 0$ ) or short timescales ( $\alpha \rightarrow 1$ ) depending on a hierarchical distribution of relaxation mechanisms [86,91]. Use of this model significantly reduces the complexity and number of parameters required to construct the material response. This simplification is not for free; however, but instead reflects an inbuilt assumption that the relaxation spectrum exhibits power-law behavior with a distribution of relaxation occurring across timescales.

In myocardial tissue, viscoelastic response can be attributed to multiple phenomena across spatiotemporal scales linked to its hierarchical structure as discussed in Section 2.1. To argue for fractional viscoelasticity, we consider a representative volume of myocardial tissue (see Fig. 2). At the microscale, the relaxation times can be relatively small reflecting the fact that friction occurs between molecules at small spatial scales. Bridging toward larger length scales, the relaxation times can increase reflecting that friction occurs between larger conglomerates of molecules or whole tissue structures. The effective density of these different mechanisms also varies across scales. Within a representative volume, we propose that the relative occurrence of these effects yields a distribution of relaxation times well-encapsulated by a fractional viscoelastic model.

Generalizing the framework in Eq. (15), the viscoelastic PK2 stress tensor can be conveniently written as a fractional viscoelastic differential equation, e.g.

$$\mathbf{S}(t) = \mathbf{S}^*(t) + \mathbf{S}_p(t), \quad \mathbf{S}^*(t) + \delta D_t^\alpha \mathbf{S}^* = \mathbf{S}_e(t) + D_t^\alpha \mathbf{S}_v, \quad (17)$$

or the analogous form,

$$\mathbf{S}(t) = \mathbf{S}_e(t) + \mathbf{S}^*(t) + \mathbf{S}_p(t), \quad \mathbf{S}^*(t) + \delta D_t^\alpha \mathbf{S}^* = D_t^\alpha \mathbf{S}_v, \quad (18)$$

where  $\mathbf{S}_p$  and  $\mathbf{S}_e$  denote the nonlinear viscoelastic and elastic responses,  $\mathbf{S}^*$  denotes the solution to the fractional differential equation, and  $\delta > 0$  is a scaling weighting the history dependence on

the PK2 stress tensor itself. Note, this is a departure from the linearity seen in the QLV model. Eq. (17) was shown to exhibit realistic viscoelastic behavior across a range of testing scenarios [35], providing advantages to the fractional form in Eq. (15). Eq. (18) performs similar to Eq. (17), with the primary difference that the model retains a purely elastic term  $\mathbf{S}_e$ .

## 2.6. A fractional viscoelastic model for the myocardium

In this paper, we propose a viscoelastic model capable of capturing the behavior of myocardial tissue. Building from Sections 2.3 to 2.4, we propose the model form shown in Eq. (18). In this case, the elastic form  $\mathbf{S}_e$  denotes the response of the underlying base structure of the tissue and is characterized by a simple neo-Hookean model with a single stiffness parameter,  $a$ , e.g.

$$\mathbf{S}_e = \frac{a}{j^{2/3}} \left( \mathbf{I} - \frac{I_C}{3} \mathbf{C}^{-1} \right). \quad (19)$$

The complex nonlinear and viscoelastic response of the tissue is incorporated through  $\mathbf{S}^*$ , which is governed by the fractional differential equation in Eq. (18). In this formulation, the underlying material response is dictated by the choice of  $\mathbf{S}_v$ , with the viscoelastic effects controlled by the parameters  $\alpha$  and  $\delta$ . Mimicking the structural forms of both *HO* and Costa models, we choose  $\mathbf{S}_v$  to be,

$$\mathbf{S}_v = \sum_{kl \in S^*} b_{kl} (\mathcal{W}_1 I_{kl} - 1) \mathbf{e}_k \otimes \mathbf{e}_l + \mathcal{W}_2 \sum_{kl \in S^+} b_{kl} I_{kl} \text{sym}(\mathbf{e}_k \otimes \mathbf{e}_l), \quad (20)$$

where  $S^* = \{\text{ff}, \text{ss}, \text{nn}\}$  and  $S^+ = \{\text{fs}, \text{fn}, \text{sn}\}$  and

$$\mathcal{W}_1(\mathbf{C}) = \exp\{b_1(I_C - 3)\}, \quad (21)$$

$$\mathcal{W}_2(\mathbf{C}) = \exp\{b_2(I_{fs}^2 + I_{fn}^2 + I_{sn}^2)\}. \quad (22)$$

More details on the selection of this model form can be found in the *Supplementary Materials*. Like the *HO* model, the first term contains an isotropic scaling,  $\mathcal{W}_1$ ; however, this term scales weighted structurally anisotropic terms. As a hyperelastic contribution, this term would lead to a diagonal matrix at the reference state, suggesting the reference state is not a stable state. However, as part of the fractional viscoelastic model (differentiated by the Caputo derivative), this is no longer a factor. Similar to the Costa model, the invariant terms are grouped, with the first term covering the sum of the diagonal invariants (note,  $I_C = I_{\text{ff}} + I_{\text{ss}} + I_{\text{nn}}$ ) and the second incorporating the shear invariants. Similar to the first term,  $\mathcal{W}_2$  scales weighted shear terms. Unlike the Costa model, weighting is done through scalings  $b_{kl}$  which are not reflected in the exponents of  $\mathcal{W}_1$  or  $\mathcal{W}_2$ . While incorporation of scalings  $b_{kl}$  into the exponential scalings of  $\mathbf{S}_v$  would make it straightforward to write as a strain-energy function, given the model is viscoelastic, this constraint is lifted. Moreover, grouping terms with two exponents,  $b_1$  and  $b_2$ , significantly simplifies the parameterization process. Last, the model considered in this paper utilizes an incompressible formulation, where  $\mathbf{S}_p = p\mathbf{J}\mathbf{C}^{-1}$ . However, other formalisms are possible to incorporate compressibility (though care must be taken when considering these forms [92]).

Important properties for constitutive models are objectivity and material frame indifference [42]. While these properties are well-known for  $\mathbf{S}_e$  and  $\mathbf{S}_p$ , for these properties to hold for  $\mathbf{S}$ , they must hold for  $\mathbf{S}^*$ . Both objectivity and material frame indifference for the proposed model are shown in Appendix A.

The proposed viscoelastic model in Eq. (18) requires 11 parameters in total. Seven constants are used to scale the isotropic and anisotropic model contributions linearly,  $\theta^l = \{a, b_{\text{ff}}, b_{\text{ss}}, b_{\text{nn}}, b_{\text{fs}}, b_{\text{fn}}, b_{\text{sn}}\}$ . The remaining four parameters – including the fractional order, the scaling on the stress in Eq. (18), and the exponen-

tial scaling parameters – have a nonlinear dependence and contribute to the nonlinear and viscoelastic response of the material  $\theta^* = \{\alpha, \delta, b_1, b_2\}$ .

## 2.7. Experimental testing of human myocardium

This modeling study relies on rheological tests performed on human myocardial samples by Sommer et al. [15,16]. While complete details on the experimental data acquisition can be found in [15,16], we reiterate the basics of data acquisition here (see Fig. 3). Briefly, human heart muscle samples were collected during transplant surgery, infused with 200mL cardioplegic solution (CPS, Celsior by Genzyme Corporation), inserted into a path of 1000 mL of CPS and cooled to 4°C. From the collected hearts, samples were cut into 25 × 25 mm<sup>2</sup> thin sheets for biaxial testing and (4 mm)<sup>3</sup> cubed samples for shear testing. Passive tests of the cardiac muscle were performed at 37°C, in a bath of CPS with 20 mM 2,3-butanedione monoxime (BDM).

Biaxial extension tests were performed on thin square specimens whose sides were aligned with the mean-fiber ( $\mathbf{e}_f$ ) and sheet directions ( $\mathbf{e}_s$ ) (Fig. 3b). Test were performed using displacement control with real-time optical measurement of sample kinematics [15]. Equibiaxial stretches ranging between 5–20% were performed, as well as non-equibiaxial stretches of varying ratios between the mean-fiber and sheet directions,  $(\mathbf{e}_f : \mathbf{e}_s) \in \{(1:1), (1:0.75), (1:0.5), (0.75:1), (0.5:1)\}$ . Four preconditioning cycles were performed before acquiring the data during the fifth cycle, at a loading speed of 3 mm/min.

Triaxial shear tests were performed on cubes extracted from adjacent locations of the biaxial samples. The cube sides were cut in order to align with the tissue microstructure (Fig. 3a). Shear deformations between 10 and 50% were performed, with a 10% increment and loading speed of 1 mm/min. Shear relaxation tests were also performed at 50% at a ramp speed of 100 mm/min and a duration of 5 min. As a cube can be used to test two orthogonal directions, a total of three specimens were needed to test all six modes of simple shear. For triaxial testing, two deformation cycles were used for preconditioning, with the data being acquired during the third cycle.

In total, 14 tests were used to fit models: 6 shear relaxation tests at 50% shear, 6 cyclic shear tests at 50% shear maximum amplitude, and fiber/cross fiber equibiaxial stretch at 10%. To verify the models, the identified parameters were used to predict the behavior of myocardium in non-equibiaxial stretch tests (fiber to sheet stretch ratios of  $\{(1:1), (1:0.75), (0.75:1), (1:0.5), (0.5:1)\}$ ) and in equibiaxial stretch at three different frequencies: 0.01, 0.033 and 0.1 Hz. Additionally, the model prediction at lower shear levels (10–40%) is compared against data acquired using two different protocols – increasing or decreasing shear levels.

## 2.8. Parameter identification and analysis

The proposed model parameters were fit to human triaxial and biaxial experimental data collected in [16], assuming idealized shear and biaxial kinematics, i.e.

$$\mathbf{F} = \gamma \mathbf{e}_k \otimes \mathbf{e}_l + \mathbf{I}, \quad \text{and} \quad \mathbf{F} = \gamma_1 \mathbf{e}_f \otimes \mathbf{e}_f + \gamma_2 \mathbf{e}_s \otimes \mathbf{e}_s + \frac{1}{\gamma_1 \gamma_2} \mathbf{e}_n \otimes \mathbf{e}_n,$$

where  $\mathbf{e}_k, \mathbf{e}_l$  denote shear along different microstructural directions, and  $\gamma, \gamma_1, \gamma_2$  denote the time dependent amount of stretch or shear applied for each test (see Fig. 3a). Here we refer to the various data tests as groups – relaxation, cyclic shear and biaxial stretch, which will be indicated by superscripts  $i \in \{r, c, b\}$ , respectively. The relaxation tests were done for each microstructural shear direction  $M^s = \{\text{fs}, \text{fn}, \text{sf}, \text{sn}, \text{nf}, \text{ns}\}$ , producing six transient Cauchy shear stress measurements,  $\sigma_{kl}$  with  $kl \in M^s$ , to compare with model based outcomes. In this case,  $\gamma = 0.5 \text{ min}(1, t)$

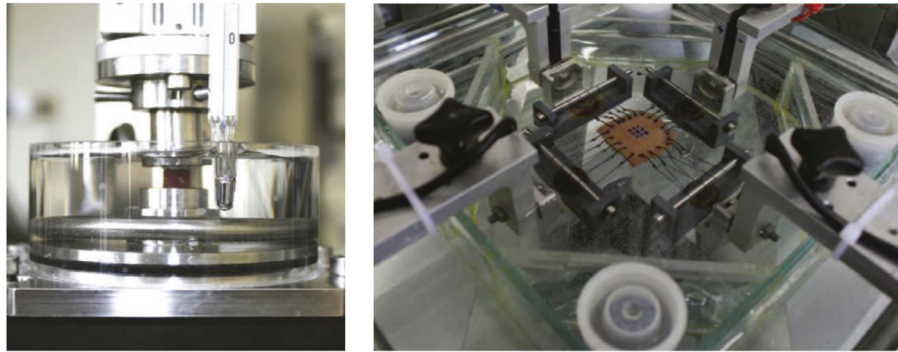
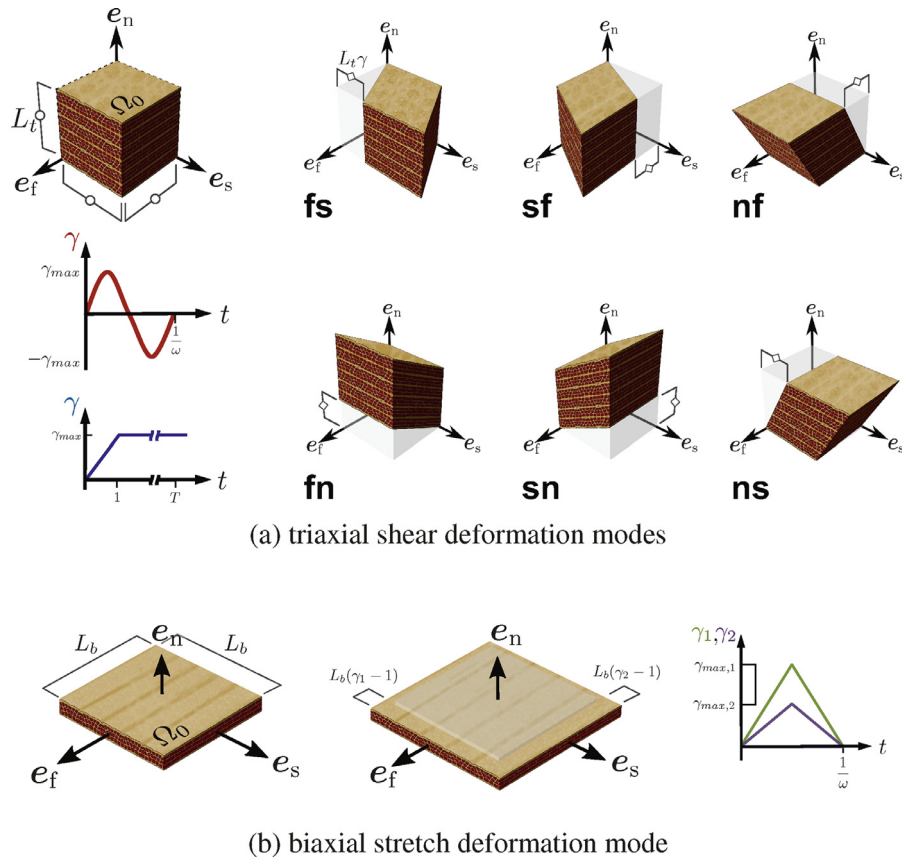


**Fig. 3.** Illustration of the experimental tests performed on human myocardial samples in [16]. (a) Reference tissue block with shear deformations applied in different directions relative to the underlying tissue microstructure. (b) Reference biaxial sample with stretch applied in fiber and sheet directions. (c) Experimental test rigs for triaxial and biaxial experiments.

as shown in Fig. 3a. Similarly, cyclic shear measurements were acquired in all shear directions  $M^S$ , resulting in an additional six transient Cauchy stress tensor measurements. In this case,  $\gamma = 0.5 \sin(\omega t)$  (see Fig. 3a), with  $\omega \approx 1.31e - 2s^{-1}$ . Simulated predictions were generated over three cycles, as in the experiment, with the final cycle used for comparisons. In addition to the cyclic shear and shear relaxation, 1:1 biaxial stretch was also considered, with  $\gamma_1 = \gamma_2 = 1 + 0.1 \sin(\sin[\omega t])$  (where  $\omega \approx 3.14e - 2s^{-1}$ ). In the biaxial tests, two transient Cauchy stress tensor measurements were acquired,  $\sigma_{kl}$  with  $kl \in M^b = \{ff, ss\}$ .

A total of 14 transient experimental measurements were used for model fitting. For each of those, let  $\sigma_{kl}^i$  denote the respective component of the Cauchy stress, with  $\bar{\sigma}_{kl}$  marking the values mea-

sured in the experiments, and  $\sigma$  the values computed using the model. The bold versions,  $\sigma_{kl}^i$  and  $\bar{\sigma}_{kl}^i$ , denote the stress over time for the  $i$ th test set and  $kl$ th stress component. Note, all models were preconditioned following the data protocol, and compared at their final cycles (where applicable).

### 2.8.1. Minimization problem

In this paper, we consider the fit of three models: the  $H0$  model, Costa model, and proposed viscoelastic model from Section 2.6. All models considered were fit to data by minimizing the objective function across all 14 tests simultaneously (Eq. (23)) to determine the model's set of  $N$ -parameters (denoted as  $\theta$ )

$$\theta = \arg \min_{y \in \mathbb{R}_+^N} \chi(y), \quad (23)$$

where the objective function,  $\chi$ , is given as

$$\chi(\mathbf{y}) = \min_{\beta \in \mathbb{R}^3} \frac{\left( \sum_{i,k,l} \left\| \frac{1}{R_{kl}^i} \left( \frac{1}{\beta^i} \sigma_{kl}^i(\mathbf{y}) - \bar{\sigma}_{kl}^i \right) \right\|_2^2 \right)^{1/2}}{\left( \sum_{i,k,l} \left\| \frac{1}{R_{kl}^i} \bar{\sigma}_{kl}^i \right\|_2^2 \right)^{1/2}}, \quad (24)$$

and  $R_{kl}^i = \|\bar{\sigma}_{kl}^i\|_2$  is introduced to give tests equivalent weights (irrespective of the magnitude or number of time points). Note that  $\chi$  gives the relative error across all tests, with  $\chi = 1$  denoting 100% error. In this minimization, a parameter set is found to best match all datasets.

In this study, the data is representative of the myocardium behavior in relaxation, cyclic shear and biaxial stretch, but it is not guaranteed to come from the same sample (e.g., for the same shear mode in relaxation and cyclic oscillations), or even from the same heart. Therefore, innate variability is introduced that may be reflective of animal to animal variability. Here we assume that the relative magnitudes test to test may vary as a result of different samples, but the shapes should be maintained. This is achieved through the introduced relative scalings  $\beta$ , which are selected to minimize the difference between model and data across all time points. In order to meaningfully preserve the anisotropy,  $\beta = (\beta^r, \beta^c, \beta^b)$  was applied across all  $kl$  directions for given tests. The selection of  $\beta$  was done iteratively with an initial guess  $\beta = \mathbf{1}$ , solving the minimization for  $\mathbf{y}$ , minimizing for  $\beta$  and repeating until convergence.

Errors were also quantified on a test by test basis to understand areas of model strength and weakness using the related test-specific objective function,

$$\chi_{kl}^i(\theta) = \min_{\beta \in \mathbb{R}^3} \frac{\left\| \frac{1}{R_{kl}^i} \left( \frac{1}{\beta^i} \sigma_{kl}^i(\theta) - \bar{\sigma}_{kl}^i \right) \right\|_2}{\left\| \frac{1}{R_{kl}^i} \bar{\sigma}_{kl}^i \right\|_2}, \quad (25)$$

where the  $\beta^i$  and  $\theta$  are determined from the minimization in Eq. (23). Minimization for the Costa and *HO* models were done using the nonlinear `lsqnonlin` minimization routine in MATLAB. Multiple initial guesses were selected for the model parameters, with the reported results selected using the best fit.

To examine the behavior and uniqueness of the parameter space of the proposed viscoelastic model, a parameter sweep was performed. To generate model predictions, each experiment had to be simulated based on the given kinematics to solve the fractional differential equation forward in time (see [35,93] for details). In this case, the model predicted response depended linearly on parameters  $\theta^l$  given a set of parameters,  $\theta^*$ . Hence, sweeping the space of all parameters (e.g.  $\mathbb{R}_+^{11}$ ) can be reduced to a sweep through the space for  $\theta^*$  (e.g.  $\mathbb{R}_+^4$ ), with a simple least squares solve applied to find the optimal parameters,  $\theta^l$ . Uniqueness of the linear parameters was then determined by the solvability of the least squares system. Because of the simple kinematics and known stresses during the relaxation tests, it was also possible to reduce the parameter space to  $\mathbb{R}_+^3$  by determining the functional relationship between  $\delta$  and  $\alpha$  during the relaxation tests. Sweeps were performed over  $b_1 \in \{0, 1, 2 \dots 20\}$ ,  $b_2 \in \{0, 0.5, 1 \dots 10\}$ , and  $\alpha \in \{0.2, 0.22, 0.24 \dots 0.4\}$  resulting in 4,851 minimizations and 67,914 test simulations. Note, a coarser sweep over higher parameter values showed continued growth in  $\chi$ . This sweep indicated that the minimum is achieved at  $\alpha = 0.24$ ,  $b_1 = 9$  and  $b_2 = 2$ . A refined sweep was then conducted around these values, as follows:  $\alpha \in \{0.2, 0.21, 0.22 \dots 0.28\}$ ,  $b_1 \in \{7, 7.5, 8 \dots 11\}$  and  $b_2 \in \{1, 1.25, 1.5 \dots 3.5\}$ .

### 2.8.2. Model sensitivity analysis

Sensitivity was assessed from two perspectives: the effect of noise in the data on the best-fit material parameters, and the effect of parameter perturbations on the fitting error. In the first instance, 100 noisy datasets were produced via adding unbiased uniformly distributed noise vector over time  $\eta$ , to the measured stress values:  $\bar{\sigma}_{kl}^i = \bar{\sigma}_{kl}^i + \eta$ . The noise level was set to 10% of the peak stress across a test for a specific mode, e.g.,  $\eta \in 0.1[-|\bar{\sigma}_{kl}^i|_\infty, |\bar{\sigma}_{kl}^i|_\infty]$ ,  $E(\eta) = 0$ . For each noisy dataset  $\bar{\sigma}_{kl}^i$ , a model fit with a different set of optimal parameters  $\theta$  were obtained, following the same parameter fit procedure. Next, the optimal parameters  $\theta_{\min}$  were perturbed by  $\pm 10\%$  of the original value, by turn. The error function  $\chi$  was computed for each local perturbation, according to Eq. (24).

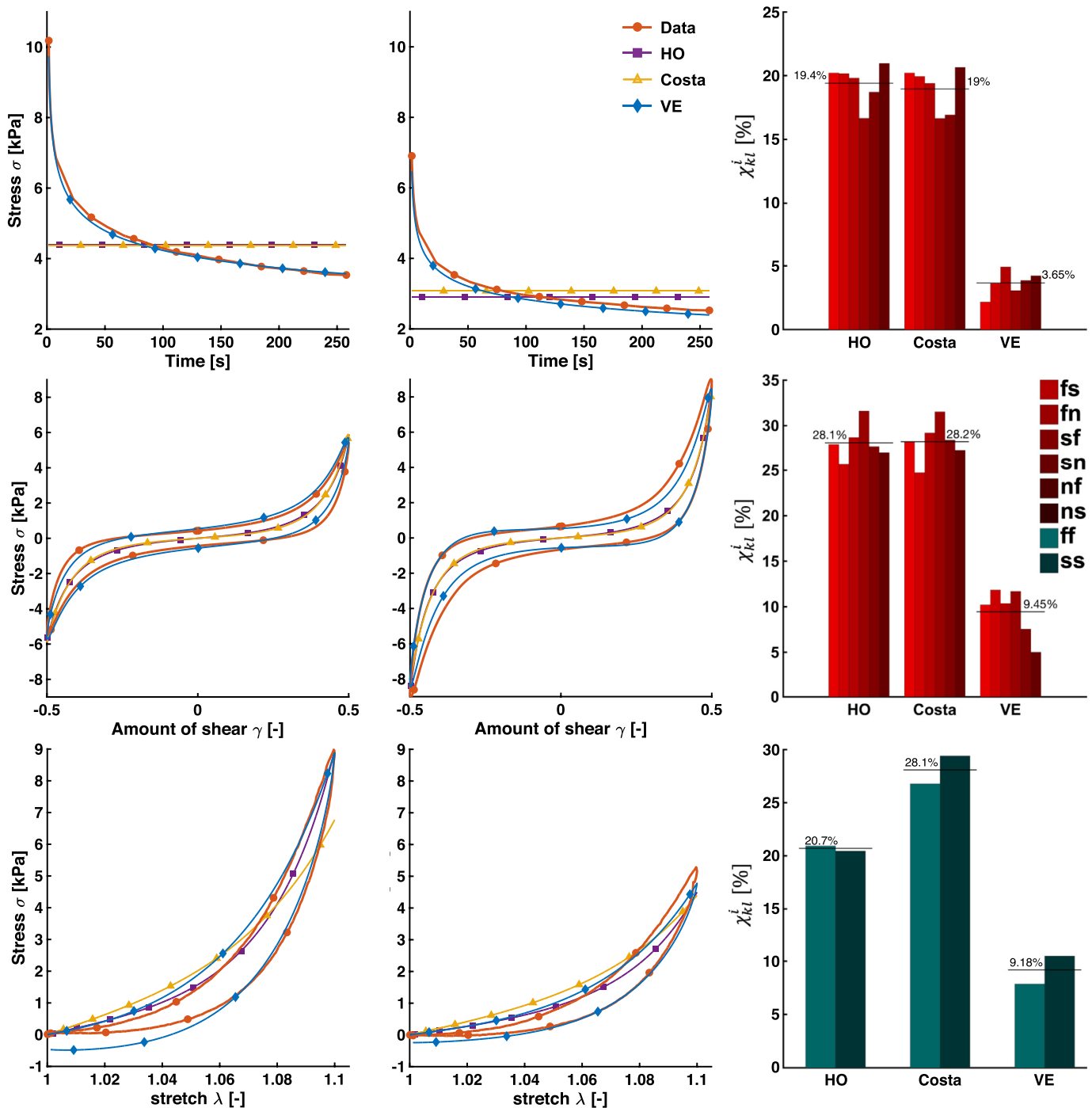
## 3. Results

Fig. 4 shows the best fit for *HO*, Costa and proposed viscoelastic (VE) models to the data. Example curves for the relaxation, cyclic shear and biaxial tests are shown along with bar plots showing test-specific errors for each of the 14 datasets, computed according to Eq. (25). The overall errors, computed using Eq. (24), were 23.73, 24.73 and 7.68% for *HO*, Costa and VE models, respectively. Here the data shows classical viscoelastic effects, with stress relaxation and hysteresis. Note that for the cyclic shear and biaxial stretch experiments, the loading curve generates a larger stress, which relaxes faster during unloading. This behavior was observed in the data and viscoelastic model.

Fig. 5 explores the VE model error across the  $\alpha$  (0.1–0.3),  $b_1$  (0–20) and  $b_2$  (0–10) parameter space. The error across all datasets, computed according to Eq. (24), is shown in the bottom right panel. The error computed separately for the relaxation, cyclic shear and biaxial tests is shown in the top left, top right and bottom left panels, respectively. Note that the linear parameters were optimized for each  $\{\alpha, b_1, b_2\}$  across all tests, and test-specific errors were plotted. The isosurfaces help visualizing the error behavior in the 3D space. In each of the four panels, the minimum error is indicated by the white sphere with the overall minimum uniquely identified at  $\alpha = 0.184$ ,  $b_1 = 10.027$  and  $b_2 = 1.158$  over all datasets. The errors over the individual tests were computed using Eq. (25).

Fig. 6 illustrates synthetic noisy datasets alongside the original data, showing the resultant noisy data for cyclic shear (fs, top left) and biaxial (top right) stretch (ff). Equivalent datasets were generated for all test cases, and replicated 100 times to examine the sensitivity of the fit to noise. For each of the 100 noisy datasets, a new set of VE linear parameters  $\theta^l$  were determined. The parameters' mean (red marker) and standard deviation (error bars) are shown relative to the original parameters, indicated by the baseline 1 (bottom right). To further understand model sensitivity to parameters, variation of the objective function was found when changing parameters by  $\pm 10\%$  (bottom left) for both linear and nonlinear parameter sets. The original parameter values can be seen in Fig. 4. The dotted line indicates the minimum model fit error of 7.68%.

Fig. 7 shows the prediction of the models under biaxial stretches of various ff:ss ratios (1:1 – blue, 1:0.75 – cyan, 0.75:1 – green, 1:0.5 – red and 0.5:1 – black). The models are shown in the top left (*HO*), top right (Costa) and bottom left (VE) panels, while the original data, from Sommer et al. [16], are presented in the bottom right panel. The solid curves indicate the fiber response, and the dashed curves show the response in sheet direction. Note that here none of the models was fit to data (except for ff:ss ratio of 1:1 which was part of the original fitting dataset), and the curves represent predictions obtained by using the parameters shown in Fig. 4.



**Fig. 4.** Constitutive model fit for *HO*, *Costa* and the proposed viscoelastic (*VE*) models, with overall error ( $\chi$ ) of 23.73, 24.73, and 7.68%, respectively. Plots comparing experimentally measured Cauchy Stress components,  $\sigma$ , with model-based predictions. Optimal parameters for *HO* were  $\{a_r, a_s, a_{fs}, a_{br}, b_s, b_{fs}, b\} = \{1.56, 0.70, 0.46, 0.61, 35.31, 33.24, 5.09, 7.50\}$ , with  $a$  parameters given in units of kPa and  $\{\beta^r, \beta^c, \beta^b\} = \{1.41, 0.74, 0.53\}$ . Optimal parameters for *Costa* were  $\{C, b_{ff}, b_{ss}, b_{nn}, b_{fs}, b_{fn}, b_{sn}\} = \{0.13, 33.27, 20.83, 2.63, 12.92, 11.99, 11.46\}$ , with  $C$  in units of kPa and  $\{\beta^r, \beta^c, \beta^b\} = \{1.37, 0.75, 0.14\}$ . Optimal parameters for *VE* were  $\{\alpha, \delta, b_1, b_2\} = \{0.184, 0.023, 10.02, 1.158\}$ ;  $\{a_e, b_{ff}, b_{ss}, b_{nn}, b_{fs}, b_{fn}, b_{sn}\} = \{0.200, 1.640, 0.897, 0.409, 6.175, 3.520, 2.895\}$  with  $a_e$  and  $b_{nn}$  in units of kPa and  $\{\beta^r, \beta^c, \beta^b\} = \{1.42, 0.81, 0.33\}$ . Model fits shown for shear relaxation (top left/center) and cyclic shear (middle left/center) in *fs* and *sf* directions and biaxial stretch (bottom left/center) in *ff* and *ss* directions, following the protocols outlined in Section 2.8. Test-specific errors,  $\chi_{kl}^i$ , are shown for the relaxation (top right), cyclic shear (middle right) and biaxial stretch (bottom right) tests for all models.

Fig. 8 shows the prediction of the viscoelastic model in *ff:ss* biaxial stretch (left), at three frequencies: 0.01, 0.033 and 0.1 Hz. The corresponding data, from the original study [16], is shown in the right panel. At 0.01 Hz, the testing conditions are identical to the biaxial test used for the model fitting. However, the data used for

the fitting and the data shown in Fig. 8 come from different samples, with the data in the frequency test reaching fiber and sheet peak amplitude smaller by a factor  $\sim 1.48$ .

Fig. 9 shows the *VE* model prediction to shear compared with data from the original study [16] on human myocardium as well

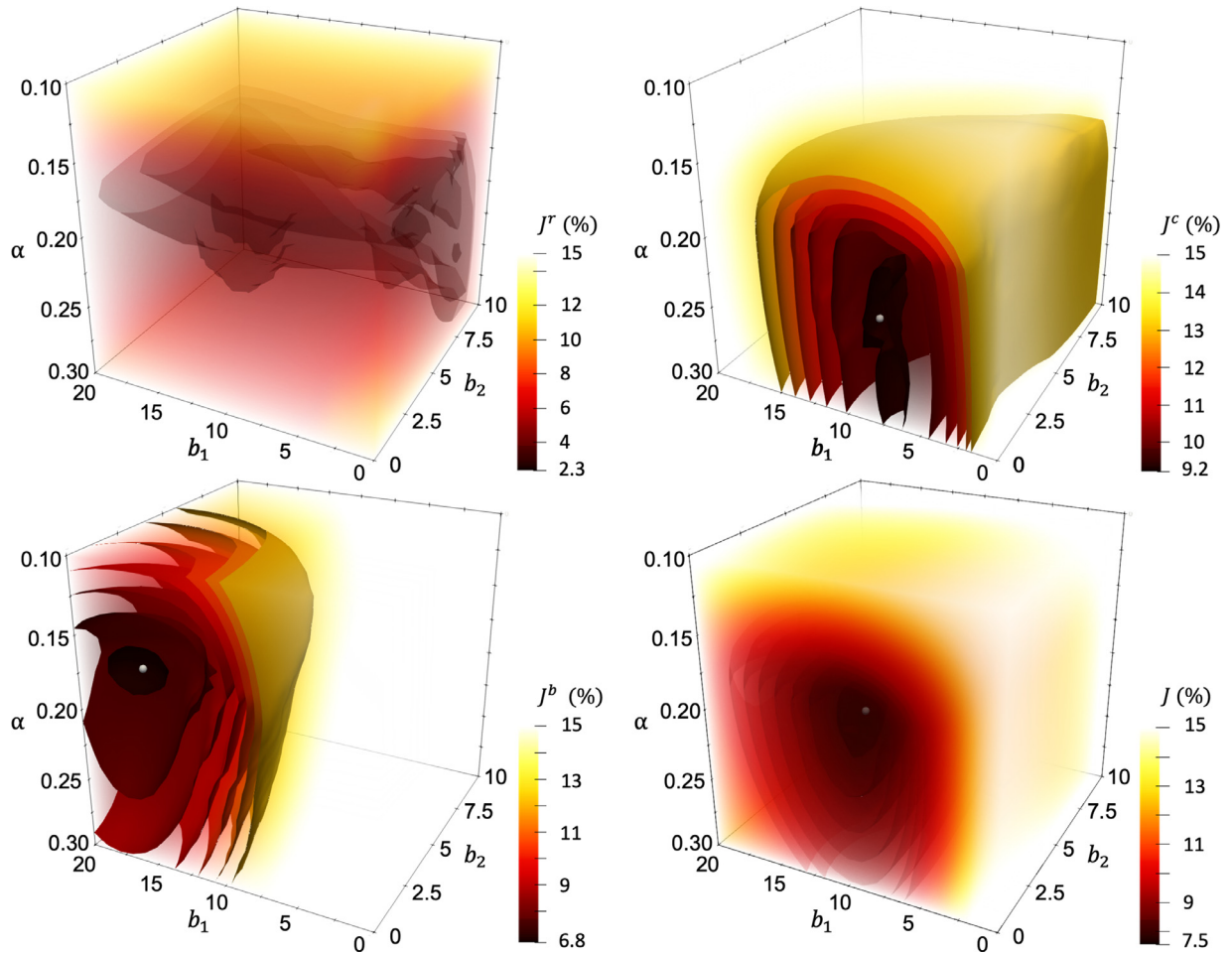


**Fig. 5.** Values of the objective function  $\chi$  across fractional order values  $\alpha \in [0, 1]$  and exponential powers  $b_1, b_2 \in [0, 20]$ . The heat maps indicate how the error changes across the 3D space. Isosurfaces are aiding in the visualisation of the error, with the white spheres indicating the location where the minimum is achieved. (Top Left) Error  $\chi^r$  across the relaxation tests only. The sweep minimum (2.65%) is achieved at  $\alpha = 0.2, b_1 = 6$  and  $b_2 = 8.5$ . (Top Right) Error  $\chi^c$  across the cyclic shear tests only. The sweep minimum (9.2%) is achieved at  $\alpha = 0.24, b_1 = 8$  and  $b_2 = 1$ . (Bottom Left) Error  $\chi^b$  across the biaxial stretch tests only. The sweep minimum (6.8%) is achieved at  $\alpha = 0.16, b_1 = 15$  and  $b_2 = 0$ . (Bottom Right) Error  $\chi$  across all tests. The minimum (7.68%) is achieved at  $\alpha = 0.184, b_1 = 10.027$  and  $b_2 = 1.158$ .

as porcine myocardium. The shear tests conducted for human myocardium start from low ( $\gamma = 0.1$ ) to high shear ( $\gamma = 0.4$ ), while the data from porcine myocardium start from high shear ( $\gamma = 0.4$ ) to low ( $\gamma = 0.1$ ). In both cases, 4-6 cycles are performed at a given shear level with the final cycle shown. Predictions from the VE model are shown (center) using the parameters presented in Fig. 4 and scaled by  $\beta^c = 0.38$ , which was determined by matching the model to original data (top row) peak amplitude in the cyclic shear test at  $\gamma = 0.4$  in the human myocardial data.

## 4. Discussion

### 4.1. Analysis of the proposed viscoelastic model

The model proposed in this work introduces viscoelasticity through a fractional approach. This choice reflects a hierarchy of relaxation times mirroring the hierarchical structure of myocardial tissue and the different spatiotemporal scales that lead to viscous dissipation. The proposed viscoelastic model presented here relies on an underlying form that combines aspects of the *HO* and Costa hyperelastic models (for more details, see the *Supplementary Material*). As in the *HO* model, the model terms used here are based on invariants that reflect the microstructural composition of the passive myocardium. However, the terms are not completely separated, allowing for coupling between invariants, as seen in Eq. (20).

Coupling of the microstructural directions is characteristic of the Costa model, where all stretches are inherently coupled. Overall, the VE model captures the characteristics of the data, as seen in representative examples of the three deformation protocols in Fig. 4. In relaxation, the model can capture the initial peak and the subsequent decay. In cyclic shear and biaxial stretch, the hysteresis and nonlinearity are well matched.

The viscoelastic model entails 11 parameters uniquely determined through the fitting process. Four of these have a nonlinear effect on the model - the fractional order  $\alpha$ , exponential powers  $b_1$  and  $b_2$  and the viscoelastic PK2 scaling  $\delta$ , while the remaining 7 parameters act as linear scalings of terms. Parameter  $\delta$  is determined from the relaxation tests, at each  $\alpha$  value, as explained in Section 2.8. For the other 3 nonlinear parameters, a sweep is carried, and at each point in the 3D space a set of 7 unique linear parameters can be identified. Fig. 5 shows the error behavior across the 3D space of the sweep. Overall, the total objective function,  $\chi$ , appears convex across the parameter space with a unique minima. To test this, nonlinear root finding was applied with 100 different random seed points distributed across parameter space ( $\alpha \in [0, 1]$ ,  $b_1 \in [0, 100]$ ,  $b_2 \in [0, 70]$ ), all of which converged to the same minima (values  $\alpha = 0.184 \pm 5.5e-4$ ,  $b_1 = 10.00 \pm 0.04$ ,  $b_2 = 1.16 \pm 0.024$ ).

Examining the breakdown of how errors from different test groups contributed to the total error, Fig. 5 shows that cyclic shear

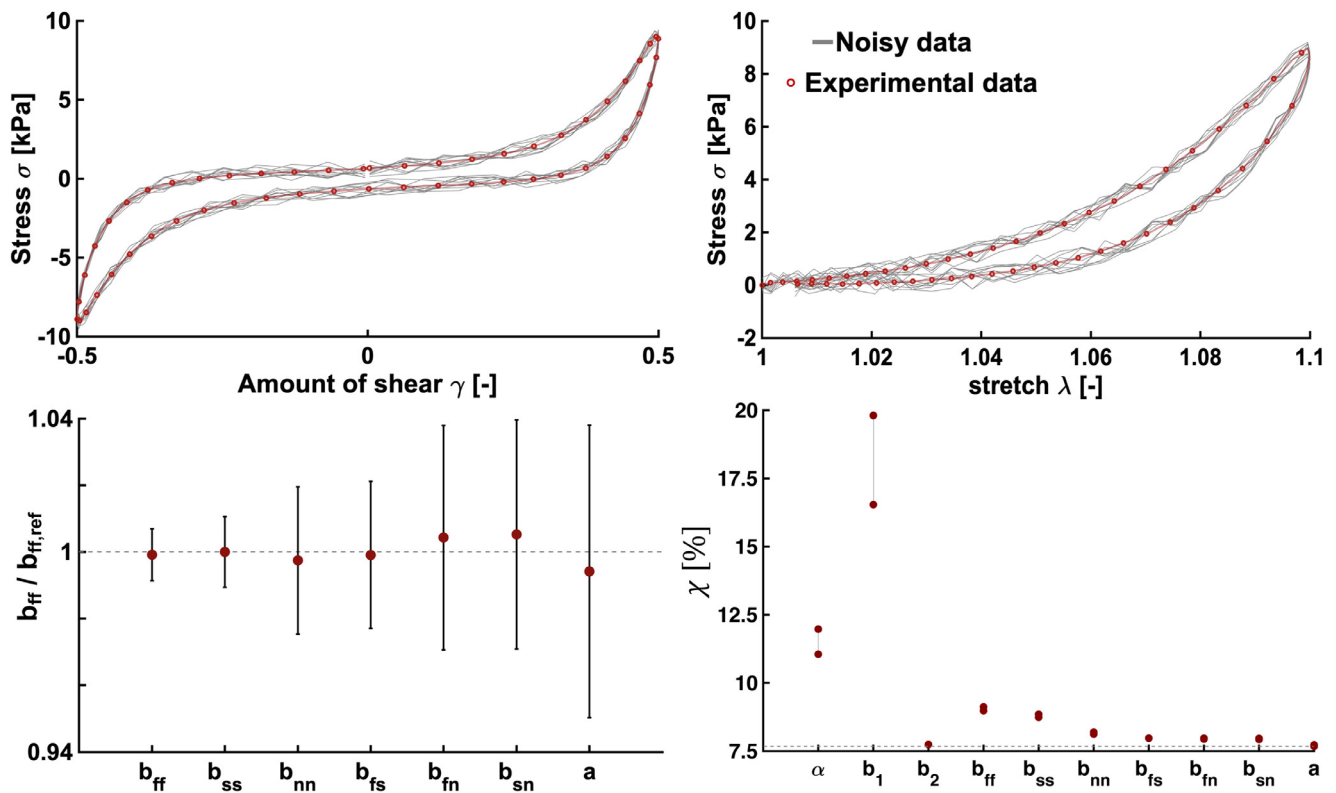


**Fig. 6.** Sample datasets for the fs and ff modes of deformation with added 10% unbiased noise compared to the original experimental data. (Top Left) Noisy data in fs cyclic shear and (Top Right) ff biaxial stretch. Plots comparing experimentally measured Cauchy Stress components,  $\sigma$ , with model-based predictions. (Bottom Left) Relative variation of model parameters obtained by fitting 100 noisy datasets. For each parameter the mean (shown as the red dot) and the range of one standard deviation (solid black line) can be compared relative to the original value (dotted line). (Bottom Right) Variation of the objective function  $\chi$  due to 10% variation in parameters. (For interpretation of the references to color in this figure, the reader is referred to the web version of this article.)

and biaxial tests both exhibit clear minima. For the relaxation tests, the objective is less specific for  $b_1$  and  $b_2$  owing to the test essentially going to a single deformation state. However, the relaxation tests exhibit a strong dependence on  $\alpha$ , with errors being small as long as  $\alpha \in [0.12, 0.25]$ . Among the three groups – relaxation, cyclic shear and biaxial, the smallest errors are achieved in relaxation, as it can be seen in both Figs. 5 and 4.

Sensitivity analysis was conducted on the viscoelastic model and its parameters. Compared to the original values (Fig. 4), the noise led to at most 4% standard deviation and averages close to the reference values, as seen in Fig. 6. This suggests that the model parameters are identifiable and robust to noise. A perturbation of  $\pm 10\%$  in  $b_{ff}$  and  $b_{ss}$  leads to the model error increase of  $\sim 1.5\%$ , while  $\pm 10\%$  perturbation of  $\alpha$  and  $b_1$  leads to a significant error increase – 3 to 11%. Importantly, all parameters alter the objective function, showing the model parameters are observable.

#### 4.2. Model-based predictive response

To examine the response of the proposed VE model, predictions of other tests not used for training were simulated, including biaxial stretch to different fiber/cross-fiber ratios (Fig. 7), frequency response (Fig. 8), and different degrees of maximal cyclic shear (Fig. 9). Applying biaxial stretch at different ratios, the proposed VE model shows excellent predictive behavior by capturing the inherent nonlinearity and hysteresis. Importantly, it also demonstrates the inherent coupling of fiber/cross-fiber stretches seen in the data, whereby change in the stretch applied in one direction influences the stress in other directions. Another predictive behavior of the VE model is shown in Fig. 8, for biaxial stretch tests at 0.01, 0.033 and 0.1 Hz. The data show that changes in frequency of one or

der of magnitude yield a modest increase in hysteresis and peak stress amplitude (up to  $\sim 19\%$ ). Modest increase in the viscoelastic model is also observed ( $\sim 41\%$ ), due to the fractional differential form. While the predictive increase is higher, this model captures this modest growth and would likely perform better with multi-frequency data created at higher frequencies.

Lastly, the VE model behavior is investigated at lower cyclic shear levels. From the original study data [16], strain softening can be observed as the shear increases with fairly sustained hysteresis, see Fig. 9 (left plot). In contrast, the proposed VE model (center plot), predicts decreased hysteresis at lower shears and nested curves that do not exhibit strain softening. However, the original data was acquired following a protocol of progressive increases in shear strain, with preconditioning cycles at each level. This means that the sample was not preconditioned to the largest shear levels until later cycles. To demonstrate this impact, the test was repeated using porcine myocardium (using the same experimental protocol) whereby the shear protocol was stepped from largest to smallest shear strain (right plot). In this case, the passive tissue response resembles that predicted by the VE model.

#### 4.3. Comparison with other models

To investigate the relative impact of the proposed VE model, results were compared with standard hyperelastic  $HO$  and Costa models (see Fig. 4). Here, hyperelastic  $HO$  and Costa models were optimized and fit using the same protocol applied to the viscoelastic model, providing a fair basis for comparison. As expected, both hyperelastic models exhibit a constant stress in relaxation and no hysteresis; however, both models do well at capturing the behavior of the data with errors of 23.73 and 24.73%. It is clear that the

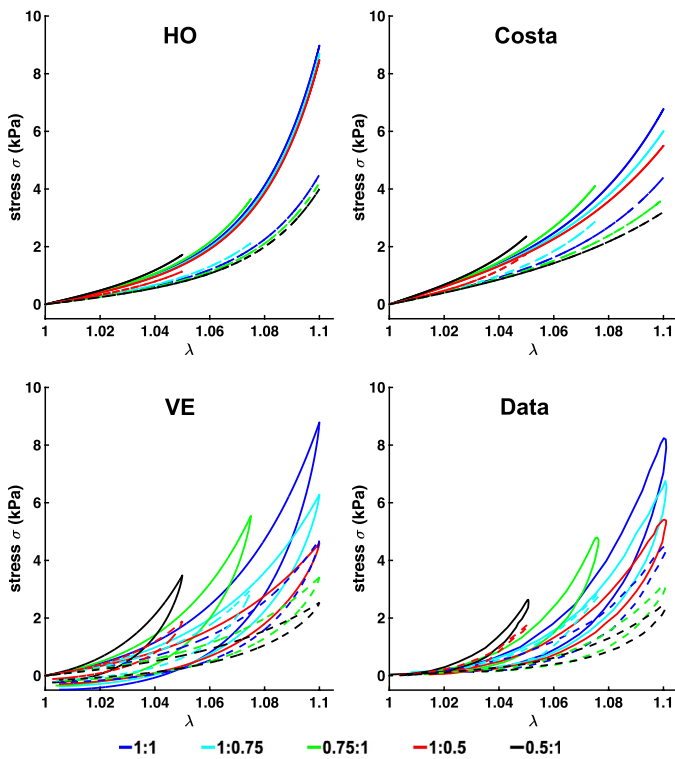


**Fig. 7.** Prediction of the models in biaxial stretch, fiber to sheet ratio ff:ss of 1:1 (blue), 1:0.75 (cyan), 0.75:1 (green), 1:0.5 (red) and 0.5:1 (black). Solid curves show the behavior in the fiber direction, and dashed curves in the sheet direction. Plots comparing experimentally measured Cauchy Stress components,  $\sigma$ , with model-based predictions. (Top left) *HO* model prediction with  $\beta^b = 0.65$ ; (Top right) Costa model prediction with  $\beta^b = 0.14$ ; (Bottom left) VE model prediction with  $\beta^b = 0.33$ ; (Bottom right) Data from the original study [16]. Note all model predictions used parameters from Fig. 4. (For interpretation of the references to color in this figure legend, the reader is referred to the web version of this article.)

loading / unloading differences observed in the data cannot be captured by the hyperelastic models, leading to elevated errors; however, fitting across all 14 datasets enables us to see how well these models can perform. It can be seen that the *HO* model performs

better in describing the nonlinear trend of the biaxial test, with the errors in this group being  $\sim 8\%$  smaller than for the Costa model. In contrast, the proposed model reduces the error metric by approximately a factor of 3 to 7.68%, with the largest reduction in relaxation tests. While these results are expected to improve (in part, due to the increase in parameters from 7 to 8 to 11), these tests provide an important benchmark for understanding the potential benefit of using a viscoelastic modeling approach. Moreover, the VE model seems to be able to better capture the shape of the curves (particularly comparing biaxial test results).

Another important comparison is with the previous viscoelastic model published by Gültekin et al. [49,94] that fits the data utilized here. This paper extended the *HO* model using a non-linear Maxwell approach [35] that relied on 18 parameters fit to each test separately. Using the results from the most recent paper [94], an analysis was performed computing our error measures on the original parameters as well as optimization of all linear material parameters (see *Supplementary Materials*). In this case, errors for the original model were 19.35% and for the re-fit model were 11.24%. Predictions from these models lack the variation in fiber / cross fiber stretch observed in the non-equibiaxial tests, and predict a significant decrease in hysteresis with increasing speed. As a result, the proposed VE model exhibits lower errors, uses fewer parameters and generally exhibits improved predictive accuracy.

Examining the predictive responses, a key observation comes when comparing the biaxial data at varying levels of stretch, see Fig. 7. In this figure, the classic *HO* model shows an uncoupling of stretch along microstructural directions, whereby loading the fiber to the same stretch and varying the stretch across fibers produces nearly the same load. This is in contrast to the Costa model and the experimental data, which show that these loads are not fully independent. In contrast, the VE model provides varying responses that qualitatively match the behavior of the data. In our testing, adding fiber dispersion to the *HO* model does show improvement; however, this tends to come at the expense of accuracy in other tests and adding these parameters did not substantially improve the model response. As this model forms the basis of that presented in [49], which shows similar challenges to these biaxial predictions, it may be insufficient to improve through inclusion of dispersion alone.

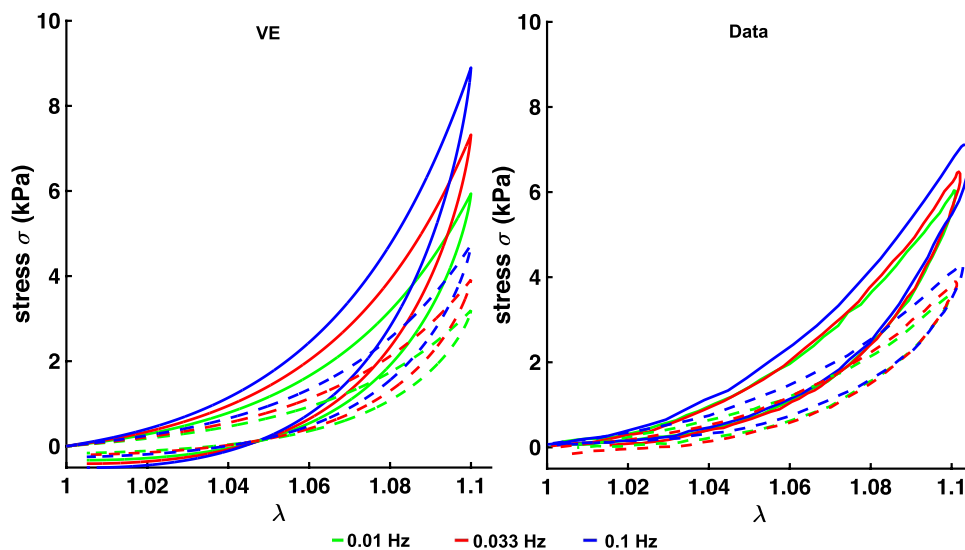


**Fig. 8.** The behavior of the proposed VE (left) against data from the original study [16] (right), in biaxial stretch tests with variable loading frequency (0.01 Hz - green, 0.033 Hz - red, 0.1 Hz - blue). Plots comparing experimentally measured Cauchy Stress components,  $\sigma$ , with model-based predictions. Solid curves show the behavior in the fiber direction, and dashed curves in the sheet direction. The model employs the parameters shown in Fig. 4 and  $\beta^b = 0.48$ . (For interpretation of the references to color in this figure legend, the reader is referred to the web version of this article.)

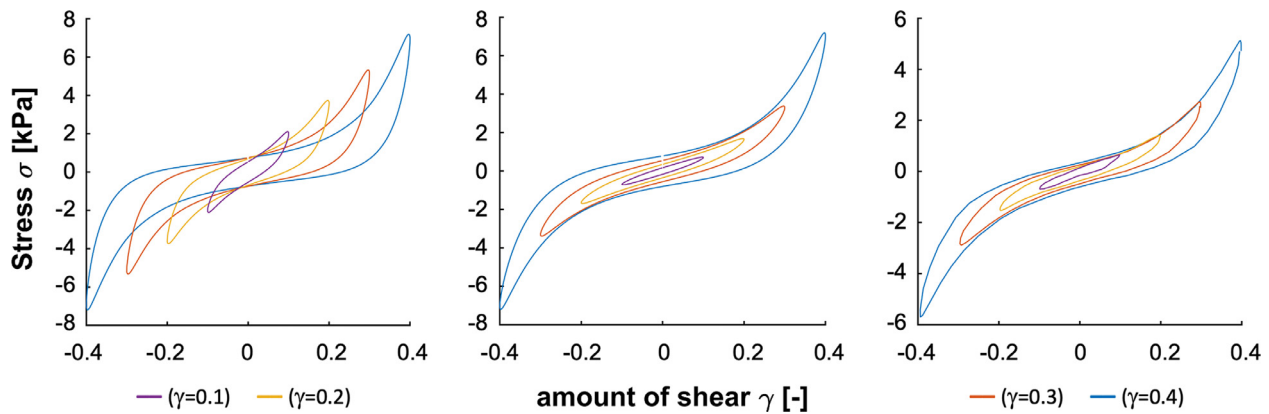


**Fig. 9.** Qualitative comparison between data and model in cyclic shear. (Left) shear at multiple levels from human myocardium [16], (center) model predictions of shear response, and (right) cyclic shear in porcine myocardium. Experiments used the same rig and protocols, with the only exception that (left) increased shear levels (pre-conditioning each level), while (right) started from higher shear, decreasing shear levels. Plots comparing experimentally measured Cauchy Stress components,  $\sigma$ , with model-based predictions.

#### 4.4. Study limitations

In this study, data from 14 tests were utilized to parameterize all models – a challenge which is often not attempted within constitutive model studies. While integration provides arguably a more complete result, the challenge comes that no tests stem from the same samples. Hence, the inherent variability in tissues make the analysis challenging. To circumvent this, all models were arbitrarily scaled based on testing groups (relaxation, cyclic shear, biaxial stretch). This allowed models to capture the essential shape, without being heavily biased by the total amplitude. An improvement to this study could be the use of new testing rigs [13], capable of providing a wide range of tests on a single sample.

In addition, idealized kinematics were used for model parameterization across all tests and constitutive equations. This assumption is commonly employed in constitutive model studies; however, it's important to note that tissue tests are often more complex. Inhomogeneity in tissue structures, microstructural orientations, presence of other structural elements (e.g. arteries) were not considered in this analysis and could alter the mechanics and kinematics. Additionally, the rheological tests performed invariably exhibit some variation from the idealized kinematics assumed. Equibiaxial displacement driven testing may not exhibit precise strains internally, particularly for anisotropic materials such as myocardium. Similarly, cyclic shear may yield non-idealized deformations due to boundary conditions, microstructural variations, mounting, amongst others. These factors could be improved in future studies through more precise regional characterization of deformations [62] as well as model-integrated parameterization [14].

While the model proposed here presents a specific form leveraging fractional viscoelasticity and tensors analogous to those from classical hyperelasticity in myocardium, we note that these forms are not unique. Numerous tensor forms were experimented with (representing  $\mathbf{S}_e$  and  $\mathbf{S}_v$ ), including nonlinear polynomial forms and more generalized split exponentials using a variety of invariants. However, other tensor forms derived from alternative hyperelastic formulations [9,22,95–97] could be worthwhile pursuing to see if further improvements in model performance could be gained. In addition, while this study focuses on the applicability of fractional viscoelasticity, many other viscoelastic formulations have been proposed – such as K-BKZ or Pipkin-Rogers forms (for review, see [42]). While the fractional model introduced shows strong fidelity and compelling predictive capacity, further exploration of viscoelastic forms may provide further gains in the modeling of myocardial tissues.

An important consideration for material models is their thermodynamic consistency, in particular, whether they satisfy the Clausius-Planck Inequality. These are often well described and defined for hyperelastic materials, but require more care when considering viscoelastic material responses. Some proofs for nonlinear viscoelastic materials [98] and linear fractional viscoelastic materials [99] have been published. Further, following the work of Following Bagley and Torvik [100], Appendix B presents an analysis demonstrating the Clausius-Planck inequality holds for the proposed anisotropic cardiac model in the oscillatory small strain limit when material parameters are strictly positive. However, a more general theory encompassing nonlinear anisotropic fractional viscoelastic models remains to be shown.

#### 5. Conclusions

In this paper, we present a nonlinear viscoelastic constitutive model for passive myocardium using a fractional approach. The model is tested against human myocardial data across a range of testing protocols, demonstrating effective reproduction of experimental measurements as well as strong prediction of other tissue measures. The model builds on the idea of cardiac viscoelasticity stemming from its hierarchical structure, yielding a spectrum of viscoelastic phenomena that span spatiotemporal scales. The model is compared with classic hyperelastic models, demonstrating a significant improvement in fitting (mean error  $\sim 7.68\%$  compared to  $\sim 24\%$ ), as well as in predictive response (particularly for variable biaxial stretch). The model also is shown to exhibit a unique set of parameters that are observable and it is robust. The proposed VE model presents one of the first constitutive models aimed at capturing viscoelastic nonlinear response across multiple testing regimes, providing a platform for better understanding the biomechanics of myocardial tissue in health and disease.

#### Declaration of Competing Interest

The authors declare that they have no known competing financial interests or personal relationships that could have appeared to influence the work reported in this paper.

#### Acknowledgments

DN acknowledges funding from the Engineering and Physical Sciences Research Council (EP/N011554/1) and the Engineering and Physical Sciences Research Council Healthcare Technology Challenge Award (EP/R003866/1), and support from the Well-

come Trust EPSRC Centre of Excellence in Medical Engineering (WT 088641/Z/09/Z) and the NIHR Biomedical Research Centre at Guy's and St.Thomas' NHS Foundation Trust and KCL. The views expressed are those of the authors and not necessarily those of the NHS, the NIHR, or the DoH.

## Appendix A. Objectivity and material frame indifference

Objectivity and material frame indifference are two important theoretical considerations for material models (see Wine-man [42] for discussion in the case of viscoelasticity). Considering objectivity, the model must exhibit a Cauchy stress tensor independent of the selected physical coordinate frame selected, making the Cauchy stress tensor a simple rotational transformation between different (rectangular Cartesian) conventions of the physical frame. Suppose an arbitrary rigid body rotation /translation is applied to the physical frame, where  $\mathbf{x}'$  denotes the rotated physical position of the body  $\mathbf{x}$  with

$$\mathbf{x}' = \mathbf{Q}(t)\mathbf{x}(\mathbf{X}, t) + \mathbf{x}_0(t)$$

where  $\mathbf{Q}(t)$  is an arbitrary orthonormal tensor with unit determinant at all times,  $t$ . In this scenario, the deformation gradient after rotation is  $\mathbf{F}' = \mathbf{Q}(t)\mathbf{F}$ . Objectivity requires that the rotated PK2 and Cauchy stresses, denoted  $\mathbf{S}'$  and  $\boldsymbol{\sigma}'$ , are related to their non-rotated forms by,

$$\mathbf{S}' = \mathbf{S}, \quad \boldsymbol{\sigma}' = \mathbf{Q}\boldsymbol{\sigma}\mathbf{Q}^T, \quad (\text{A.1})$$

It remains to show that either conditions of Eq. (A.1) hold for the proposed material model. Noting that  $\mathbf{Q}^T\mathbf{Q} = \mathbf{I}$ , we can see that  $\mathbf{C}' = (\mathbf{F}')^T\mathbf{F}' = \mathbf{C}$  and, moreover, any invariants from Eqs. (1) to (3) are equivalent. Hence,  $\mathbf{S}'_e = \mathbf{S}_e$  and  $\mathbf{S}'_p = \mathbf{S}_p$ . What remains from Eq. (18) is to prove  $\mathbf{S}'^* = \mathbf{S}^*$ . Noting that the anisotropic invariants of  $\mathbf{C}$  are equivalent, and rotations do not alter microstructural vectors in the reference frame, we can see that  $\mathbf{S}'_v = \mathbf{S}_v$  and, as a consequence of Eq. (18),  $\mathbf{S}'^* = \mathbf{S}^*$ .

Material frame indifference is the idea that the material response should be independent of the selection of the material frame, making the PK2 stress tensor a simple rotational transformation between (rectangular Cartesian) material frames. Suppose we rotate the material frame by the orthonormal transform,  $\mathbf{H}$ , making a new reference frame  $\mathbf{X}^* = \mathbf{H}\mathbf{X}$ . In this case, the rotated PK2 stress tensor and Cauchy stress tensor, denoted  $\mathbf{S}^*$  and  $\boldsymbol{\sigma}^*$ , are related to their non-rotated forms by,

$$\mathbf{S}^* = \mathbf{H}\mathbf{S}\mathbf{H}^T, \quad \boldsymbol{\sigma}^* = \boldsymbol{\sigma}, \quad (\text{A.2})$$

where  $\mathbf{S}^* = \mathbf{S}^*(\mathbf{C}^*, \mathbf{e}_i^*)$  and  $\mathbf{S} = \mathbf{S}(\mathbf{C}, \mathbf{e}_i)$ . As in the case of objectivity, it suffices to show one of these conditions holds. Noting that  $\mathbf{H}^T\mathbf{H} = \mathbf{I}$  and  $\mathbf{F}^* = \nabla_{\mathbf{X}^*}\mathbf{x}^* = \mathbf{H}\mathbf{F}$ , it can be shown that right Cauchy Green strains are related by rotation  $\mathbf{C}^* = \mathbf{H}\mathbf{C}\mathbf{H}^T$ . As a result, all isotropic invariants of  $\mathbf{C}$  in Eq. (1) are equivalent to their  $\mathbf{C}^*$  counterparts. Similarly, since  $\mathbf{e}_i^* = \mathbf{H}\mathbf{e}_i$ , anisotropic invariants from Eq. (3) maintain equivalence. Maintaining conditions in Eq. (A.2) on  $\mathbf{S}^*$  requires that these conditions hold for  $\mathbf{S}^*_e, \mathbf{S}^*_p$  and  $\mathbf{S}^*_v$ . The first two are satisfied (noting  $\mathbf{H}^{-1} = \mathbf{H}^T$ ), leaving determination of this property on  $\mathbf{S}^*_v$ . From the fractional differential equation in Eq. (18) (and noting that  $\mathbf{H}$  commutes with the Caputo derivative),  $\mathbf{S}^*_v = \mathbf{H}\mathbf{S}_v\mathbf{H}^T$  when

$$\mathbf{S}^*_v + \delta D_t^\alpha \mathbf{S}^*_v = \mathbf{H}D_t^\alpha (\mathbf{S}_v)\mathbf{H}^T = D_t^\alpha (\mathbf{H}\mathbf{S}_v\mathbf{H}^T) = D_t^\alpha \mathbf{S}^*_v.$$

Hence, material frame indifference holds for  $\mathbf{S}^*$  if it holds for  $\mathbf{S}_v$ . This can be verified by noting that  $\mathcal{W}_1$  and  $\mathcal{W}_2$  remain equivalent (based on equivalence of invariants) and microstructural directions,  $\mathbf{e}_i^* = \mathbf{H}\mathbf{e}_i$ .

## Appendix B. Clausius-Planck inequality for oscillatory small strain limit

Following Bagley and Torvik [100], we consider the case of small strain cyclic oscillatory loading in the myocardial model. In this case, we suppose that the displacement and pressure may be written as

$$\mathbf{u}(\mathbf{X}, t) = \mathbf{U}_0(\mathbf{X}) \sin(\omega t), \quad |\nabla_{\mathbf{X}}\mathbf{U}_0| \leq \gamma \ll 1,$$

$$p(\mathbf{X}, t) = \text{Re}\{p_0(\mathbf{X}) \exp(i\omega t)\},$$

where  $\omega > 0$  is the frequency of oscillation,  $\mathbf{U}_0 : \Omega_0 \rightarrow \mathbb{R}^3$  encodes the spatial solution of displacement, and  $p_0 : \Omega_0 \rightarrow \mathbb{C}$  encodes the spatial solution of pressure (which may be out of phase with the displacements).

Considering the Clausius-Planck inequality for an isothermal process, the material's internal energy and and power must satisfy,

$$\mathcal{D}_{\text{loc}} = -\rho \dot{\psi} + \frac{1}{2} \mathbf{S} : \dot{\mathbf{C}} \geq 0, \quad (1)$$

where  $\mathcal{D}_{\text{loc}}$  denotes the local dissipation and  $\psi$  denotes the free energy. Bagley and Torvik [100] use this condition to argue that under these kinematic conditions that: (1) any increasing component of the power  $\mathcal{P} = \frac{1}{2} \mathbf{S} : \dot{\mathbf{C}}$  must be strictly positive, and (2) that the integral of the power must be greater or equal to zero for all time.

Considering the model introduced in Section 2.6, we start by considering the linearization (noting that  $\gamma \ll 1$ ), the right Cauchy Green strain tensor can be simplified to

$$\mathbf{C} = 2\boldsymbol{\varepsilon} + \mathbf{I} + \mathcal{O}(\gamma^2), \quad \dot{\mathbf{C}} = 2\dot{\boldsymbol{\varepsilon}} + \mathcal{O}(\gamma^2), \quad \mathbf{C}^{-1} = \mathbf{I} - 2\boldsymbol{\varepsilon} + \mathcal{O}(\gamma^2)$$

where

$$\boldsymbol{\varepsilon} = \frac{1}{2} (\nabla_{\mathbf{X}}\mathbf{u} + \nabla_{\mathbf{X}}\mathbf{u}^T), = \boldsymbol{\varepsilon}_0 \sin(\omega t),$$

denotes the small strain tensor. Similarly, the determinant can be linearized

$$J = 1 + \nabla_{\mathbf{X}} \cdot \mathbf{u} + \mathcal{O}(\gamma^2)$$

which, assuming incompressibility, implies that

$$\nabla_{\mathbf{X}} \cdot \mathbf{U}_0 = 0, \quad \boldsymbol{\varepsilon} : \mathbf{I} = 0.$$

Considering the material invariants of  $\mathbf{C}$ ,

$$I_{\mathbf{C}} = \text{tr}(2\boldsymbol{\varepsilon} + \mathbf{I}) + \mathcal{O}(\gamma^2) = 3 + \mathcal{O}(\gamma^2)$$

$$I_{\text{kl}} = 2I_{\text{kl},\boldsymbol{\varepsilon}} + \delta_{\text{kl}} + \mathcal{O}(\gamma^2)$$

Leveraging these linearized kinematic quantities, we can examine the impact on the material kinetics quantities. Considering the elastic and hydrostatic components, we observe that

$$\mathbf{S}_e + \mathbf{S}_p = 2a\boldsymbol{\varepsilon} + p(\mathbf{I} - 2\boldsymbol{\varepsilon}) + \mathcal{O}(\gamma^2)$$

Using a power series expansion of the exponential, we can see that  $\mathcal{W}_1 = 1 + \mathcal{O}(\gamma^2)$  and  $\mathcal{W}_2 = 1 + \mathcal{O}(\gamma^2)$ . Consequently, the viscous stress tensor,  $\mathbf{S}_v$ , becomes

$$\mathbf{S}_v = \sum_{\text{kl} \in \text{SUS}^+} b_{\text{kl}} (2I_{\text{kl},\boldsymbol{\varepsilon}} - \delta_{\text{kl}}) \text{sym}(\mathbf{e}_{\text{k}} \otimes \mathbf{e}_{\text{l}})$$

Looking at the periodic steady-state response of  $\mathbf{S}^*$  (as  $t \gg 1$ ), let  $\mathbf{S}^*(\mathbf{X}, t) = \text{Re}\{\mathbf{S}_0(\mathbf{X}) \exp(i\omega t)\}$  (where  $\mathbf{S}_0 : \Omega_0 \rightarrow \mathbb{C}^{3 \times 3}$ ), and noting  $\boldsymbol{\varepsilon} = -\text{Re}\{i\boldsymbol{\varepsilon}_0 \exp(i\omega t)\}$ ,

$$\mathbf{S}_0 + \delta(i\omega)^\alpha \mathbf{S}_0 = (i\omega)^\alpha \sum_{\text{kl} \in \text{SUS}^+} 2b_{\text{kl}} I_{\text{kl},\boldsymbol{\varepsilon}_0} \text{sym}(\mathbf{e}_{\text{k}} \otimes \mathbf{e}_{\text{l}})$$

making the temporal evolution of  $\mathbf{S}^*$  defined as,

$$\mathbf{S}^* = [B \cos(\omega t) + A \sin(\omega t)] \sum_{\text{kl} \in \text{SUS}^+} 2b_{\text{kl}} I_{\text{kl},\boldsymbol{\varepsilon}_0} \text{sym}(\mathbf{e}_{\text{k}} \otimes \mathbf{e}_{\text{l}})$$

with

$$A = \omega^\alpha \frac{\delta\omega^\alpha + \cos(\frac{\pi}{2}\alpha)}{1 + 2\delta\omega^\alpha \cos(\frac{\pi}{2}\alpha) + (\delta\omega^\alpha)^2},$$

$$B = \omega^\alpha \frac{\sin(\frac{\pi}{2}\alpha)}{1 + 2\delta\omega^\alpha \cos(\frac{\pi}{2}\alpha) + (\delta\omega^\alpha)^2}.$$

Examining the power production within the cardiac viscoelastic model, we can see that

$$\begin{aligned} \mathcal{P} &= \frac{1}{2} \mathbf{S} : \dot{\mathbf{C}}, \\ &= \frac{1}{2} [\mathbf{S}_e + \mathbf{S}_p + \mathbf{S}^*] : [2\dot{\boldsymbol{\epsilon}} + \mathcal{O}(\gamma^2)], \\ &= 2a\boldsymbol{\epsilon} : \dot{\boldsymbol{\epsilon}} + p(\mathbf{I} - 2\boldsymbol{\epsilon}) : \dot{\boldsymbol{\epsilon}} + \mathbf{S}^* : \dot{\boldsymbol{\epsilon}} + \mathcal{O}(\gamma^2), \\ &= (2a|\boldsymbol{\epsilon}_0|^2 + AK) \sin(\omega t) \cos(\omega t) + BK \cos^2(\omega t), \end{aligned}$$

with  $K = \sum_{kl \in \text{SUS}} 2b_{kl} (I_{kl, \boldsymbol{\epsilon}_0})^2$ .

As a result, the power has a dissipating growth ensuring the appropriate sign of  $\mathcal{D}_{\text{loc}}$  if  $BK \geq 0$ , and has strictly positive integrated power if  $(2a|\boldsymbol{\epsilon}_0|^2 + AK) \geq 0$ . A sufficient condition that satisfies these inequalities is the requirement that all parameters ( $a, \delta, b_{kl}$ ) are strictly positive. In this case, the model is consistent with the Clausius-Planck inequality in Eq. (B.1).

## Supplementary material

Supplementary material associated with this article can be found, in the online version, at doi:10.1016/j.actbio.2021.08.036.

## References

- [1] M.R. Zile, C.F. Baicu, W.H. Gaasch, Diastolic heart failure – abnormalities in active relaxation and passive stiffness of the left ventricle, *New Engl. J. Med.* 350 (19) (2004) 1953–1959.
- [2] K. Sharma, D.A. Kass, Heart failure with preserved ejection fraction, *Circ. Res.* 115 (1) (2014) 79–96.
- [3] J.P. Cleutjens, E.E. Creemers, Integration of concepts: cardiac extracellular matrix remodeling after myocardial infarction, *J. Card. Fail.* 8 (6) (2002) S344–S348.
- [4] R. Chabiniok, V.Y. Wang, M. Hadjicharalambous, L. Asner, J. Lee, M. Sermesant, E. Kuhl, A.A. Young, P. Moireau, M.P. Nash, D. Chapelle, D.A. Nordsletten, Multiphysics and multiscale modelling, data-model fusion and integration of organ physiology in the clinic: ventricular cardiac mechanics, *Interface Focus* 6 (2) (2016) 1–24.
- [5] M. Blix, Die Länge und die Spannung des Muskels, *Skand. Arch. Physiol.* 3 (1) (1892) 295–318.
- [6] R.H. Woods, A few applications of a physical theorem to membranes in the human body in a state of tension, *Trans. R. Acad. Med. Irel.* 10 (1) (1892) 417–427.
- [7] J.G. Pinto, Y. Fung, Mechanical properties of the heart muscle in the passive state, *J. Biomech.* 6 (6) (1973) 597–616.
- [8] L.L. Demer, F. Yin, Passive biaxial mechanical properties of isolated canine myocardium, *J. Physiol.* 339 (1) (1983) 615–630.
- [9] J.D. Humphrey, R.K. Strumpf, F.C.P. Yin, Determination of a constitutive relation for passive myocardium: I. A new functional form, *J. Biomech. Eng.* 112 (3) (1990) 333–339.
- [10] F.C. Yin, R.K. Strumpf, P.H. Chew, S.L. Zeger, Quantification of the mechanical properties of noncontracting canine myocardium under simultaneous biaxial loading, *J. Biomech.* 20 (6) (1987) 577–589.
- [11] S. Dokos, I.J. LeGrice, B.H. Smaill, J. Kar, A.A. Young, A triaxial-measurement shear-test device for soft biological tissues, *J. Biomech. Eng.* 122 (5) (2000) 471–478.
- [12] S. Dokos, B.H. Smaill, A.A. Young, I.J. LeGrice, Shear properties of passive ventricular myocardium, *Am. J. Physiol. Heart Circ. Physiol.* 283 (6) (2002) H2650–H2659.
- [13] R. Avazmohammadi, D.S. Li, T. Leahy, E. Shih, J.S. Soares, J.H. Gorman, R.C. Gorman, M.S. Sacks, An integrated inverse model-experimental approach to determine soft tissue three-dimensional constitutive parameters: application to post-infarcted myocardium, *Biomech. Model. Mechanobiol.* 17 (1) (2018) 31–53.
- [14] D.S. Li, R. Avazmohammadi, S.S. Merchant, T. Kawamura, E.W. Hsu, J.H. Gorman III, R.C. Gorman, M.S. Sacks, Insights into the passive mechanical behavior of left ventricular myocardium using a robust constitutive model based on full 3D kinematics, *J. Mech. Behav. Biomed. Mater.* 103 (2020) 103508.
- [15] G. Sommer, D.C. Haspinger, M. Andrä, M. Sacherer, C. Viertler, P. Regitnig, G.A. Holzapfel, Quantification of shear deformations and corresponding stresses in the biaxially tested human myocardium, *Ann. Thorac. Surg. Biomed. Eng.* (2015) 1–15.
- [16] G. Sommer, A.J. Schriefel, M. Andrä, M. Sacherer, C. Viertler, H. Wolinski, G.A. Holzapfel, Biomechanical properties and microstructure of human ventricular myocardium, *Acta Biomater.* 24 (2015) 172–192.
- [17] J. Bonet, R. Wood, *Nonlinear Continuum Mechanics for Finite Element Analysis*, Cambridge University Press, 1997.
- [18] G.A. Holzapfel, *Nonlinear Solid Mechanics: a Continuum Approach for Engineering science*, John Wiley & Sons Ltd, 2000.
- [19] C. Truesdell, W. Noll, *The Non-Linear Field Theories of Mechanics*, Springer, 2004.
- [20] J.M. Guccione, A.D. McCulloch, L. Waldman, Passive material properties of intact ventricular myocardium determined from a cylindrical model, *J. Biomech. Eng.* 113 (1) (1991) 42–55.
- [21] J. Humphrey, F. Yin, Biomechanical experiments on excised myocardium: theoretical considerations, *J. Biomech.* 22 (4) (1989) 377–383.
- [22] J.D. Humphrey, R.K. Strumpf, F.C.P. Yin, Determination of a constitutive relation for passive myocardium: II. Parameter estimation, *J. Biomech. Eng.* 112 (3) (1990) 340–346.
- [23] K.D. Costa, J.W. Holmes, A.D. McCulloch, Modelling cardiac mechanical properties in three dimensions, *Philos. Trans. R. Soc. Lond. Ser. A Math. Phys. Eng. Sci.* 359 (1783) (2001) 1233–1250.
- [24] G.A. Holzapfel, R.W. Ogden, Constitutive modelling of passive myocardium: a structurally based framework for material characterization, *Philos. Trans. R. Soc. Lond. Math. Phys. Eng. Sci.* 367 (1902) (2009) 3445–3475.
- [25] H. Schmid, M. Nash, A. Young, P. Hunter, Myocardial material parameter estimation – a comparative study for simple shear, *J. Biomech. Eng.* 128 (5) (2006) 742–750.
- [26] H. Schmid, P. O’Callaghan, M. Nash, W. Lin, I. LeGrice, B. Smaill, A. Young, P. Hunter, Myocardial material parameter estimation, *Biomech. Model. Mechanobiol.* 7 (3) (2008) 161–173.
- [27] M. Blix, Die Länge und die Spannung des Muskels, *Skand. Arch. Physiol.* 4 (1) (1893) 399–409.
- [28] M. Blix, Die Länge und die Spannung des Muskels, *Skand. Arch. Physiol.* 5 (1) (1894) 173–206.
- [29] A. Hill, W. Hartree, The thermo-elastic properties of muscle, *Philos. Trans. R. Soc. Lond. Ser. B Contain. Pap. Biol. Character* 210 (1921) 153–173.
- [30] A. Levin, J. Wyman, The viscous elastic properties of muscle, *Proc. R. Soc. Lond. Ser. B Contain. Pap. Biol. Character* 101 (709) (1927) 218–243.
- [31] S.M. Walker, Potentiation and hysteresis induced by stretch and subsequent release of papillary muscle of the dog, *Am. J. Physiol. Leg. Content* 198 (3) (1960) 519–522.
- [32] J.K. Leach, R.S. Alexander, Effect of epinephrine on stress relaxation and distensibility of the isolated cat heart, *Am. J. Physiol. Leg. Content* 209 (5) (1965) 935–940.
- [33] L. O’Brien, J. Remington, Time course of pressure changes following quick stretch in tortoise ventricle, *Am. J. Physiol. Leg. Content* 211 (3) (1966) 770–776.
- [34] M.M. Lewinter, R. Engler, R.S. Pavelec, Time-dependent shifts of the left ventricular diastolic filling relationship in conscious dogs, *Circ. Res.* 45 (5) (1979) 641–653.
- [35] W. Zhang, A. Capilnasiu, D. Nordsletten, Comparative analysis of nonlinear viscoelastic models across common biomechanical experiments, *J. Elast.* (2021) 1–36.
- [36] E.H. Dill, *Continuum Mechanics: Elasticity, Plasticity, Viscoelasticity*, CRC Press, 2006.
- [37] Y.C. Fung, *Biomechanics: Mechanical Properties of Living Tissues*, Springer Science & Business Media, 2013.
- [38] F. Wilhelm, *Viscoelasticity*, Springer-Verlag, London, 1975. T975
- [39] B.D. Coleman, W. Noll, Foundations of linear viscoelasticity, *Rev. Mod. Phys.* 33 (2) (1961) 239.
- [40] W. Noll, A mathematical theory of the mechanical behavior of continuous media, *Arch. Ration. Mech. Anal.* 2 (1) (1958) 197–226.
- [41] A. Pipkin, T. Rogers, A non-linear integral representation for viscoelastic behaviour, *J. Mech. Phys. Solids* 16 (1) (1968) 59–72.
- [42] A. Wineman, Nonlinear viscoelastic solids: a review, *Math. Mech. Solids* 14 (3) (2009) 300–366.
- [43] J. Simo, On a fully three-dimensional finite-strain viscoelastic damage model: formulation and computational aspects, *Comput. Methods Appl. Mech. Eng.* 60 (2) (1987) 153–173.
- [44] G.A. Holzapfel, On large strain viscoelasticity: continuum formulation and finite element applications to elastomeric structures, *Int. J. Numer. Methods Eng.* 39 (22) (1996) 3903–3926.
- [45] G.A. Holzapfel, T.C. Gasser, A viscoelastic model for fiber-reinforced composites at finite strains: continuum basis, computational aspects and applications, *Comput. Methods Appl. Mech. Eng.* 190 (34) (2001) 4379–4403.
- [46] G.A. Holzapfel, J.C. Simo, A new viscoelastic constitutive model for continuous media at finite thermomechanical changes, *Int. J. Solids Struct.* 33 (20) (1996) 3019–3034.
- [47] J.M. Huyghe, D.H. van Campen, T. Arts, R.M. Heethaar, The constitutive behaviour of passive heart muscle tissue: a Quasi-linear viscoelastic formulation, *J. Biomech.* 24 (9) (1991) 841–849.
- [48] F.B.C. Cansız, H. Dal, M. Kaliske, An orthotropic viscoelastic material model for passive myocardium: theory and algorithmic treatment, *Comput. Methods Biomech. Biomed. Eng.* 18 (11) (2015) 1160–1172.
- [49] O. Gültekin, G. Sommer, G.A. Holzapfel, An orthotropic viscoelastic model for the passive myocardium: continuum basis and numerical treatment, *Comput. Methods Biomech. Biomed. Eng.* (2016) 1–18.

- [50] S. Holm, *Waves with Power-Law Attenuation*, Springer, 2019.
- [51] R.L. Magin, *Fractional Calculus in Bioengineering*, Vol. 2, Begell House Redding, 2006.
- [52] M. Yang, L.A. Taber, The possible role of poroelasticity in the apparent viscoelastic behavior of passive cardiac muscle, *J. Biomech.* 24 (7) (1991) 587–597.
- [53] E.U. Azeloglu, M.B. Albro, V.A. Thimmappa, G.A. Ateshian, K.D. Costa, Heterogeneous transmural proteoglycan distribution provides a mechanism for regulating residual stresses in the aorta, *Am. J. Physiol. Heart Circ. Physiol.* 294 (3) (2008) H1197–H1205.
- [54] F.S. Cavalcante, S. Ito, K. Brewer, H. Sakai, A.M. Alencar, M.P. Almeida, J.S. Andrade Jr, A. Majumdar, E.P. Ingenito, B. Suki, Mechanical interactions between collagen and proteoglycans: implications for the stability of lung tissue, *J. Appl. Physiol.* 98 (2) (2005) 672–679.
- [55] X. Guo, Y. Lanir, G.S. Kassab, Effect of osmolarity on the zero-stress state and mechanical properties of aorta, *Am. J. Physiol. Heart Circ. Physiol.* 293 (4) (2007) H2328–H2334.
- [56] P.P. de Tombe, H.T. Keurs, An internal viscous element limits unloaded velocity of sarcomere shortening in rat myocardium, *J. Physiol.* 454 (1992) 619.
- [57] Z.L. Shen, H. Kahn, R. Ballarini, S.J. Eppell, Viscoelastic properties of isolated collagen fibrils, *Biophys. J.* 100 (12) (2011) 3008–3015.
- [58] S. Meghezi, F. Couet, P. Chevallier, D. Mantovani, Effects of a pseudophysiological environment on the elastic and viscoelastic properties of collagen gels, *Int. J. Biomater.* 2012 (2012) 1–9, doi:10.1155/2012/319290.
- [59] A.M. Reeve, M.P. Nash, A.J. Taberner, P.M. Nielsen, Constitutive relations for pressure-driven stiffening in poroelastic tissues, *J. Biomech. Eng.* 136 (8) (2014) 081011.
- [60] A.C. Hoskins, A. Jacques, S.C. Bardswell, W.J. McKenna, V. Tsang, C.G. dos Remedios, E. Ehler, K. Adams, S. Jalilzadeh, M. Avkiran, et al., Normal passive viscoelasticity but abnormal myofibrillar force generation in human hypertrophic cardiomyopathy, *J. Mol. Cell. Cardiol.* 49 (5) (2010) 737–745.
- [61] O. Lieleg, M.M. Claessens, A.R. Bausch, Structure and dynamics of cross-linked actin networks, *Soft Matter* 6 (2) (2010) 218–225.
- [62] C. Witzenburg, R. Raghupathy, S.M. Kren, D.A. Taylor, V.H. Barocas, Mechanical changes in the rat right ventricle with decellularization, *J. Biomech.* 45 (5) (2012) 842–849.
- [63] I. LeGrice, A. Pope, B. Smaill, The architecture of the heart: myocyte organization and the cardiac extracellular matrix, in: *Interstitial Fibrosis in Heart Failure*, Springer, 2005, pp. 3–21.
- [64] P.P. Lunkenheimer, K. Redmann, P. Westermann, K. Rothaus, C.W. Cryer, P. Niederer, R.H. Anderson, The myocardium and its fibrous matrix working in concert as a spatially netted mesh: a critical review of the purported tertiary structure of the ventricular mass, *Eur. J. Cardio Thorac. Surg.* 29 (Supplement 1) (2006) S41–S49.
- [65] S.M. Weis, J.L. Emery, K.D. Becker, D.J.M. Bride, J.H. Omens, A.D. McCulloch, Myocardial mechanics and collagen structure in the osteogenesis imperfecta murine (oim), *Circ. Res.* 87 (8) (2000) 663–669.
- [66] P. Fratzl, *Collagen: Structure and Mechanics*, Springer Science & Business Media, 2008.
- [67] J.E. Bishop, G. Lindahl, Regulation of cardiovascular collagen synthesis by mechanical load, *Cardiovasc. Res.* 42 (1) (1999) 27–44.
- [68] P. Fratzl, K. Misof, I. Zizak, G. Rapp, H. Amenitsch, S. Bernstorff, Fibrillar structure and mechanical properties of collagen, *J. Struct. Biol.* 122 (1) (1998) 119–122.
- [69] R. Puxkandl, I. Zizak, O. Paris, J. Keckes, W. Tesch, S. Bernstorff, P. Purslow, P. Fratzl, Viscoelastic properties of collagen: synchrotron radiation investigations and structural model, *Philos. Trans. R. Soc. Lond. B Biol. Sci.* 357 (1418) (2002) 191–197.
- [70] S. Hayes, C.S. Kamma-Lorger, C. Boote, R.D. Young, A.J. Quantock, A. Rost, Y. Khatib, J. Harris, N. Yagi, N. Terrill, et al., The effect of riboflavin/uvra collagen cross-linking therapy on the structure and hydrodynamic behaviour of the ungulate and rabbit corneal stroma, *PLoS One* 8 (1) (2013) e52860.
- [71] P.J. Hanley, A.A. Young, I.J. LeGrice, S.G. Edgar, D.S. Loiselle, 3-dimensional configuration of perimysial collagen fibres in rat cardiac muscle at resting and extended sarcomere lengths, *J. Physiol.* 517 (3) (1999) 831–837.
- [72] P.P. Purslow, Strain-induced reorientation of an intramuscular connective tissue network: implications for passive muscle elasticity, *J. Biomech.* 22 (1) (1989) 21–31.
- [73] P.P. Purslow, The extracellular matrix of skeletal and cardiac muscle, in: P. Fratzl (Ed.), *Collagen: Structure and Function*, Springer, 2008, pp. 325–357.
- [74] H. Mori, K. Shimizu, M. Hara, Dynamic viscoelastic properties of collagen gels in the presence and absence of collagen fibrils, *Mater. Sci. Eng. C* 32 (7) (2012) 2007–2016.
- [75] H. Mori, K. Shimizu, M. Hara, Dynamic viscoelastic properties of collagen gels with high mechanical strength, *Mater. Sci. Eng. C* 33 (6) (2013) 3230–3236.
- [76] R.M. Irastorza, B. Drouin, E. Blangino, D. Mantovani, Mathematical modeling of uniaxial mechanical properties of collagen gel scaffolds for vascular tissue engineering, *Sci. World J.* 2015 (2015) 1–9, doi:10.1155/2015/859416.
- [77] H. Li, Y. Zhang, Modeling of the viscoelastic behavior of collagen gel from dynamic oscillatory shear measurements, *Biorheology* 51 (6) (2015) 369–380.
- [78] B. Xu, H. Li, Y. Zhang, An experimental and modeling study of the viscoelastic behavior of collagen gel, *J. Biomech. Eng.* 135 (5) (2013) 054501.
- [79] B. Xu, H. Li, Y. Zhang, Understanding the viscoelastic behavior of collagen matrices through relaxation time distribution spectrum, *Biomater* 3 (3) (2013) e24651.
- [80] R.W. Ogden, *Non-Linear Elastic Deformations*, Dover Publications, 2013.
- [81] R. Avazmohammadi, J.S. Soares, D.S. Li, T. Eperjesi, J. Pilla, R.C. Gorman, M.S. Sacks, On the in vivo systolic compressibility of left ventricular free wall myocardium in the normal and infarcted heart, *J. Biomech.* 107 (2020) 109767.
- [82] I.J. LeGrice, B.H. Smaill, L.Z. Chai, S.G. Edgar, J.B. Gavin, P.J. Hunter, Lamina structure of the heart: ventricular myocyte arrangement and connective tissue architecture in the dog, *Am. J. Physiol. Heart Circ. Physiol.* 269 (2) (1995) H571–H582.
- [83] M. Hadjicharalambous, R. Chabiniok, L. Asner, E. Sammut, J. Wong, G. Carr-White, J. Lee, R. Razavi, N. Smith, D. Nordsletten, Analysis of passive cardiac constitutive laws for parameter estimation using 3D tagged MRI, *Biomech. Model. Mechanobiol.* 14 (4) (2015) 807–828.
- [84] F. Mainardi, *Fractional Calculus and Waves in Linear Viscoelasticity: an Introduction to Mathematical Models*, World Scientific, 2010.
- [85] K. Adolfsson, M. Enelund, Fractional derivative viscoelasticity at large deformations, *Nonlinear Dyn.* 33 (3) (2003) 301–321.
- [86] H. Schiessel, R. Metzler, A. Blumen, T. Nonnenmacher, Generalized viscoelastic models: their fractional equations with solutions, *J. Phys. A Math. Gen.* 28 (1995) 6567–6584.
- [87] N. Tschoegl, *The Phenomenological Theory of Linear Viscoelastic Behavior*, vol. 1, Springer-Verlag Heidelberg, 1989.
- [88] Ingolf Sack, Korinna Jöhrens, Jens Würfel, Braun Jürgen, Structure-sensitive elastography: on the viscoelastic powerlaw behavior of in vivo human tissue in health and disease, *Soft Matter* 9 (24) (2013) 5672–5680.
- [89] K.J. Parker, T. Szabo, S. Holm, Towards a consensus on rheological models for elastography in soft tissues, *Physics in Medicine & Biology* 64 (21) (2019) 1–17.
- [90] I. Podlubny, *Fractional differential equations: an introduction to fractional derivatives, Fractional Differential Equations, to Methods of their Solution and some of their Applications*, vol. 198, Academic press, 1998.
- [91] H. Schiessel, A. Blumen, Hierarchical analogues to fractional relaxation equations, *Journal of Physics A: Mathematical and General* 26 (19) (1993) 5057–5069.
- [92] D.R. Nolan, A.L. Gower, M. Destrade, R.W. Ogden, J.P. McGarry, A robust anisotropic hyperelastic formulation for the modelling of soft tissue, *J. Mech. Behav. Biomed. Mater.* 39 (2014) 48–60.
- [93] W. Zhang, A. Capilnasiu, G. Sommer, G.A. Holzapfel, D.A. Nordsletten, An efficient and accurate method for modeling nonlinear fractional viscoelastic biomaterials, *Comput. Methods Appl. Mech. Eng.* 362 (2020) 112834.
- [94] O. Gültekin, H. Dal, Computational Finite Strain Orthotropic Viscoelasticity of Human Passive Myocardium, in: *Solid (Bio)mechanics: Challenges of the Next Decade*. A book dedicated to Professor Gerhard A. Holzapfel, Springer, 2021, pp. 269–290.
- [95] J.D. Humphrey, F.C.P. Yin, On Constitutive Relations and Finite Deformations of Passive Cardiac Tissue: I. A Pseudostrain-Energy Function, *Journal of Biomechanical Engineering* 109 (4) (1987) 298–304.
- [96] John C Criscione, Andrew S Douglas, William C Hunter, Physically based strain invariant set for materials exhibiting transversely isotropic behavior, *Journal of the Mechanics and Physics of Solids* 49 (4) (2001) 871–897.
- [97] R.C.P. Kerckhoffs, P.H.M. Bovendeerd, J.C.S. Kotte, F.W. Prinzen, K. Smits, T. Arts, Homogeneity of cardiac contraction despite physiological asynchrony of depolarization: a model study, *Annals of Biomedical Engineering* 31 (5) (2003) 536–547.
- [98] Harold Benjamin, Michel Destrade, William J Parnell, On the thermodynamic consistency of Quasi-linear viscoelastic models for soft solids, *Mechanics Research Communications* 111 (2021) 1–6.
- [99] Alexander Lion, On the thermodynamics of fractional damping elements, *Continuum Mechanics and Thermodynamics* 9 (2) (1997) 83–96.
- [100] R.L. Bagley, P.J. Torvik, On the Fractional Calculus Model of Viscoelastic Behavior, *Journal of Rheology* 30 (1) (1986) 133–155.
- [101] H.G. Benedicto, P.P. Bombonato, G. Macchiarelli, G. Stifano, I.M. Prado, Structural arrangement of the cardiac collagen fibers of healthy and diabetic dogs, *Microsc. Res. Tech.* 74 (11) (2011) 1018–1023.
- [102] G. Macchiarelli, O. Ohtani, S. Nottola, T. Stallone, A. Camboni, I. Prado, P. Motta, A micro-anatomical model of the distribution of myocardial endomysial collagen, *Histol. Histopathol.* 17 (2002) 699–706.